

Análise Estrutural da Bacia do Parnaíba através da Função do Receptor e das Curvas de Dispersão calculadas a partir de Terremotos e Ruído Sísmico Ambiental



Orientando:
Diogo Luiz de Oliveira Coelho
Orientador:
Jordi Julià Casas

Exame de Qualificação submetido ao Programa de Pesquisa e Pós-Graduação em Geodinâmica e Geofísica - PPGG, da Universidade Federal do Rio Grande do Norte - UFRN, como requisito à obtenção do Título de Doutor em Geodinâmica e Geofísica

Natal, Brasil 2017

Resumo

A gênese e evolução de grandes bacias sedimentares no interior de continentes estáveis é um importante problema geológico que não é facilmente compreendido dentro do paradigma da Tectônica de Placas. A bacia do Parnaíba é uma das três grandes bacias sedimentares Paleozóicas na plataforma Sulamericana - junto com as bacias do Paraná e Amazonas. A bacia é comumente descrita como uma grande bacia cratônica do tipo sag com uma forma semi-circular e um depocentro que chega a profundidades de 3.5 km. Já o mecanismo físico que atuou na sua subsidência e evolução, em contrapartida, é muito controverso. Vários mecanismos de formação foram propostos nessa bacia, mas o conhecimento sobre a arquitetura crustal e mantélica abaixo da bacia do Parnaíba ainda é muito pequeno. Devido a isso, nós propomos investigar a arquitetura crustal abaixo da bacia do Parnaíba através da análise das Funções do Receptor e da tomografia de ruído ambiental, para imagear estruturas profundas e rasas, respectivamente. Na primeira parte do nosso trabalho, nós apresentamos estimativas pontuais de espessura crustal e razão V_p/V_s em 9 estações numa transecta NW-SE na parte central da bacia, junto com perfis de velocidade de onda S obtidos na inversão conjunta entre funções do receptor e velocidades de ondas de superfície. Essa análise revela a crosta como sendo espessa com 44-45 km em média no depocentro e um afinamento progressivo de 39-41 km em direção às bordas, enquanto que a razão V_p/V_s varia entre 1.70 e 1.78 ao longo da transecta, com grandes valores próximo ao depocentro. Os perfis de velocidade confirmam essa variação da espessura crustal e revelam uma crosta inferior de 18-22 km de profundidade com velocidades variando de 3.7 a 3.8 km/s, mas que podem chegar a 4.0-4.2 km/s perto do depocentro. Nossos resultados favorecem modelos de formação de bacia que possuem um estiramento crustal mínimo e são compatíveis com dobramentos flexurais devido a uma carga em profundidade. No entanto, não se observa a existência de um grande corpo intrusivo na crosta inferior. Arguimos que processos convectivos profundos na astenosfera podem prover tal mecanismo de carga. A segunda parte do nosso trabalho consistirá no imageamento da zona de transição do manto com funções de receptor para ver qual

o comportamento da astenosfera abaixo da bacia. Além disso, utilizaremos o ruído ambiental para analisar as estruturas crustais rasas, principalmente para entender o efeito do lineamento Transbrasiliano na formação da bacia.

Abstract

The genesis and evolution of large basins in the stable interiors of continents is an important geological problem that is not easily understood within the Plate Tectonics paradigm. The Parnaíba basin is one of three large Paleozoic basins in stable South America - together with the Paraná and Amazon basin. The basin is commonly described as a large, sag-type cratonic basin, with a roughly circular shape and a depocenter reaching up to 3.5 km depth. The physical mechanism behind its subsidence and evolution, on the other hand, is more controversial. A number of basin-forming mechanisms have been proposed for this basin, but the knowledge about the deep architecture of this cratonic basin is very little yet. Owing to that, we propose to investigate the crustal and mantle architecture beneath of the Parnaíba basin by analyzing P-wave receiver functions and ambient noise tomography, to image deep and shallow structures, respectively. In the first part of our work, we present point estimates of crustal thickness and Vp/Vs ratio at 9 broadband stations in a 600 km-long transect crossing the central portion of the basin, along with detailed S-wave velocity-depth profiles obtained from the joint inversion of P-wave receiver functions and surface-wave dispersion velocities. This analysis reveals the crust could be as thick as 44-45 km around the basin's depocenter and that it progressively thins to 39-41 km towards the edges, while bulk Vp/Vs ratios are in the 1.70-1.78 range along the transect, with larger values around the depocenter. The velocity-depth profiles confirm crustal thickness variations and reveal a lower crustal layer below 18-22 km depth, with S-velocities in the 3.7-3.8 km/s range that locally raise to 4.0-4.2 km/s near the depocenter. Our findings favor models invoking minimal stretching of the basin's underlying crust and are found compatible with flexural bending by a deep load. However, the existence of a thick intrusive body pervading the lower crust is not supported by our results. We argue that deep convective processes in the asthenosphere might provide an alternative loading mechanism. The second part of our work will consist of imaging the transition zone of the mantle with P-wave receiver functions to see how is the behavior of the asthenosphere beneath the basin. Further-

more, to use the ambient noise to analyse the shallow crustal structures of the basin, mainly to understand the Transbrasiliano lineament effect in the basin evolution.

Conteúdo

| | |
|--|-----|
| Resumo | i |
| Abstract | iii |
| 1 Introdução | 1 |
| 1.1 Escopo | 1 |
| 1.2 Objetivos | 1 |
| 1.3 Justificativa | 2 |
| 1.4 Cronograma de Execução | 3 |
| 2 Modelos de Formação de Bacias Intracratônicas | 5 |
| 3 Arcabouço Geológico da Bacia do Parnaíba | 7 |
| 3.1 Preenchimento Sedimentar | 7 |
| 3.2 Magmatismo | 9 |
| 3.3 Tectônica | 10 |
| 4 Artigo: Deep crustal architecture of the Parnaíba basin of NE Brazil from receiver function analysis: Implications for basin subsidence | 12 |
| 5 Artigo: Receiver function imaging of mantle transition zone discontinuities beneath Parnaíba Basin | 53 |
| 6 Artigo: Ambient noise tomography across Parnaíba Basin | 55 |
| Bibliografia | 57 |

Capítulo 1

Introdução

1.1 Escopo

Este exame de qualificação está estruturado em seis partes. A primeira parte trata da apresentação do tema, com objetivos, justificativas e as estapas propostas no projeto de doutorado que foram concluídas, ou não. A segunda parte compõe um breve resumo sobre o paradigma da formação e evolução de bacias intracratônicas. A terceira parte apresenta a síntese do arcabouço geológico da Bacia do Parnaíba, mostrando um sumário sobre o preenchimento sedimentar, magmatismo e tectônica proposta em trabalhos anteriores. A quarta parte apresenta um artigo intitulado: *"Deep crustal architecture of the Parnaíba basin of NE Brazil from receiver function analysis: Implications for basin subsidence"* que foi submetido para a The Geological Society Special Publications em março deste ano. A quinta e sexta partes propõem temas a serem estudados nos próximos semestre, como descontinuidades mantélicas de 410 km e 660 km através das funções do receptor e a tomografia de ruído sísmico ambiental, respectivamente.

1.2 Objetivos

Esta tese de doutorado tem por objetivo principal a caracterização estrutural, tanto crustal quanto mantélica, da Bacia do Parnaíba para buscar informações nesse arcabouço estrutural sobre os processos de formação e evolução na bacia. Com essa finalidade, foram elaborados objetivos secundários:

1. Determinação das estruturas crustais profundas na bacia através das estimativas pontuais de espessura crustal e razão V_p/V_s junto com perfis de velocidade de onda S obtidos na inversão conjunta entre funções do receptor e velocidades de ondas de superfície;

2. Imageamento das descontinuidades mantélicas de 410 km e 660 km, limites inferior e superior da Zona de Transição, para entender o papel da temperatura na evolução geológica da bacia;
3. Imagear o lineamento Transbrasiliense dentro da bacia através da tomografia de ruído sísmico ambiental para entender o papel dessa mega-estrutura na formação e evolução da bacia;
4. Gerar subsídios para a proposição de um modelo de formação e evolução da Bacia do Parnaíba.

1.3 Justificativa

A Bacia do Parnaíba, mesmo com um grande número de trabalhos realizados recentemente, ainda carece de muita informação sobre seu arcabouço estrutural crustal e mantélico. Esta bacia é tomada como paradigma para compreender porque grandes áreas no interior de continentes, consideradas estáveis, em certos momentos de sua história passam por longos estágios de subsidência, ao longo dos quais são acumulados pacotes de rochas sedimentares com vários quilômetros de espessura associadas a manifestações vulcânicas episódicas. A maior parte do conhecimento sobre esta bacia é restrito a escala continental, como os estudos de Feng et al. [2004], Feng et al. [2007], Lloyd et al. [2010], van der Meijde et al. [2013], Assumpção et al. [2013a], Assumpção et al. [2013b], Goutorbe et al. [2015] e Uieda and Barbosa [2017], e mais recentemente trabalhos regionais como os de de Castro et al. [2014], Daly et al. [2014], de Castro et al. [2016] e Tozer et al. [2017].

O presente trabalho encontra-se vinculado ao *Parnaíba Basin Analysis Project*, uma parceria entre a BP Energy do Brasil e várias universidades no Brasil e no Reino Unido, e tem com o objetivo melhorar o conhecimento sobre a origem e evolução dessa grande bacia cratônica no Norte-Nordeste do Brasil. Tal bacia é considerada uma fronteira exploratória, devido a descoberta de campos de gás natural durante a última década. Devido à sua grande dimensão, a maior parte do substrato sobre o qual a Bacia do Parnaíba se desenvolveu encontra-se encoberta, de forma que as informações disponíveis advêm majoritariamente de forma indireta. A análise conjunta de dados sismológicos, oriundos de sismos e de ruído ambiental, possibilita uma melhor resolução na observação de estruturas profundas e rasas no interior da bacia.

1.4 Cronograma de Execução

Após realizar as disciplinas propostas no projeto de Doutorado e ter um coeficiente de rendimento médio superior a 4, as únicas componentes curriculares obrigatórias pendentes são: Seminário de Pesquisa II, Exame de Qualificação, Exame de Proficiência em outra língua estrangueira diferente de inglês e Tese de Doutorado. Dos quais o Seminário de Pesquisa II e Exame de Qualificação eu já me encontro matriculado e devo cumprir no fim desse semestre. Restando apenas um exame de proficiência que devo cumprir no começo do próximo semestre e, por fim, a Defesa da Tese no final de 2018.

| 2015 | | |
|---|-------------|-------------|
| Atividade | - | 2º Semestre |
| GGF2045 - METODOS MATEMATICOS APLICADOS | - | Aproveitada |
| GGF3014 - PROBLEMAS GEOFÍSICOS INVERSOS | - | Aproveitada |
| GGF2012 - SISMOLOGIA | - | |
| GGF2038 - NEOTECTONICA | - | |
| Revisão Bibliográfica | - | |
| Trabalho de Campo | - | Red |
| 2016 | | |
| Atividade | 1º Semestre | 2º Semestre |
| GGF2013 - APPLICACOES SISMOLOGICAS | Black | |
| GGF2021 - TOPICOS EM GEOFISICA II | Black | |
| GGF3007 - TOPICOS AVANCIADOS EM SISMOLOGIA | Black | |
| GGF2011 - ELEMENTOS DE TECTONOFISICA | | Black |
| GGF2047 - TECTONICA DE BACIAS SEDIMENTARES | | Black |
| GGF3007 - TOPICOS AVANCIADOS EM SISMOLOGIA | | Black |
| Processamento de Dados da Função do Receptor | Black | |
| Processamento das Curvas de Dispersão (Eventos) | | Red |
| Revisão Bibliográfica | Black | Red |
| Trabalho de Campo | Black | Red |
| 2017 | | |
| Atividade | 1º Semestre | 2º Semestre |
| GGF3001 - SEMINARIO DE PESQUISA II | | Black |
| GGF6000 - EXAME DE PROFICIÊNCIA EM INGLÊS | | Black |
| GGF8000 - EXAME DE QUALIFICAÇÃO DE DOUTORADO | | Black |
| Análise dos Dados da Função do Receptor | Black | |
| Processamento das Curvas de Dispersão (Eventos) | Black | Red |
| Processamento da Inversão Conjunta | Black | Black |
| Processamento das Curvas de Dispersão (Ruído) | | Red |
| Revisão Bibliográfica | Black | Red |
| Trabalho de Campo | Black | Red |
| Submissão Artigo I | Black | White |
| 2018 | | |
| Atividade | 1º Semestre | 2º Semestre |
| GGF6000 - EXAME DE PROFICIÊNCIA EM ESPANHOL | Grey | |
| Análise dos Dados da Função do Receptor | Grey | |
| Processamento das Curvas de Dispersão (Ruído) | Grey | |
| Revisão Bibliográfica | Grey | |
| Tomografia de Ruído | | Grey |
| Processamento da Inversão Conjunta | | Grey |
| Submissão Artigo II | Grey | White |
| Submissão Artigo III | | Grey |
| Trabalho de Campo | Grey | White |
| Defesa de Doutorado | | Grey |

Figura 1.1: Cronograma proposto no projeto de Doutorado. Preto - Etapas concluídas, Vermelho - etapas não concluídas na época proposta, Cinza - Etapas futuras

Capítulo 2

Modelos de Formação de Bacias Intracratônicas

Allen and Armitage [2012] utiliza o termo bacia cratônica para com as bacias localizadas distantes de margens continentais convergentes e localizados numa variedade de substratos crustais, independentemente de serem escudos cristalinos, cinturões de dobramentos antigos e riftes complexos. Segundo Armitage and Allen [2010], pode-se considerar que o interior dos continentes não sofre com a convecção do manto subjacente e com a tectônica de placas operante. No entanto, grandes regiões da litosfera continental estável tem experimentado ciclos de subsidência prolongada e de soerguimento, gerando grandes bacias. A principal feição das bacias cratônicas é o seu período de subsidência prolongada, o qual se iniciaria durante períodos de dispersão continental e podem continuar através de ciclos de fechamento de oceanos e colisão continental. Elas estão situadas no interior de margens passivas, mas são comumente conectadas ao oceano por riftes falhados que estão orientados em alto ângulo com a margem da placa, possíveis braços abortados de junções tríplices.

Allen and Armitage [2012] mostra que apesar das individualidades de cada bacia, existem várias feições estruturais que podem ser comuns entre as bacias cratônicas, como: (1) a área da superfície ao redor da isópaca zero do preenchimento sedimentar é comumente circular ou elíptica; (2) em corte essas bacias possuem formato de pinhas, mostrando uma falta de falhas sin-tectônicas e uma espessura sedimentar menor que 5 km de profundidade; (3) a duração da subsidência é muito longa, por volta de centenas de milhões de anos, e as curvas de subsidência tectônica oriundas do backstripping apresentam uma tendência sublinear a um exponencial negativo suave. Essa longevidade da subsidência geralmente compreende várias fases de deposição da bacia separadas por inconformidades, gerando megasequências sobrepostas, que são

produtos das mudanças na tectônica operante na época de deposição; (4) a estratigrafia é predominantemente de ambiente terrestre a marinho-raso, indicando que a sedimentação acompanhou o ritmo da subsidência tectônica. As bacias cratônicas em baixas paleolatitudes são geralmente dominadas por sedimentos quimiogênicos, mostrando que o suprimento de sedimento em partículas era modesto, e que altos topográficos estavam ausentes em torno das margens das bacias nesses locais; (5) bacias cratônicas são comumente espaçadas regularmente com seus centros localizados cerca de 10^3 km de distância das bordas; (6) algumas bacias cratônicas estão associadas com o magmatismos amplamente difundidos, como a erupção de grandes volumes de basaltos. No entanto, as ligações entre o vulcanismo e o desenvolvimento da bacia ainda não são claras.

Existem inúmeras tentativas de explicar a origem e o desenvolvimento de grandes bacias sedimentares intracratônicas extensas e longevas, como pode ser visto nos trabalhos de Hartley and Allen [1994], Kaminski and Jaupart [2000], Armitage and Allen [2010], McKenzie and Priestley [2016]. O preenchimento sedimentar desse tipo de bacia raramente mostra-se falhado, sugerindo que deformação frágil raramente acompanha a subsidência. Hartley and Allen [1994] propõem que a baixa a moderada maturidade dos indicadores termais nos sedimentos da bacia não está associada com as principais distorções termais da litosfera. Existiram dois períodos na história da Terra quando a iniciação de bacias cratônicas tem sido importantes, ambos relacionados com a quebra de assembléias supercontinentais. As bacias cratônicas antigas das quais se possuem mais dados são as pertencentes ao Craton norte-americano, que são associadas com a quebra do continente Laurâncio no começo do Paleozóico, como observado no trabalho de Kaminski and Jaupart [2000].

Hartley and Allen [1994] e Allen and Armitage [2012] enumeram as hipóteses propostas na literatura para explicar a criação e evolução das bacias intracratônicas, como (1) estiramento litosférico seguido de uma contração termal, (2) mudanças de fase crustais e mantélicas, metamorfismo e intrusão, (3) tensão planar ou rejuvenescimento tectônico, (4) instabilidades convectivas no manto, e (5) erosão subaérea de estruturas soerguidas. No entanto, uma melhor compreensão dos mecanismos de formação das bacias cratônicas é dificultada pela falta de conhecimento de algumas condições pretéritas das bacias. Além disso, o momento atual é um dispersão continental em vez de uma de ruptura supercontinental, como resultado, as bacias cratônicas podem ser características menos comuns da superfície da Terra hoje, quando comparadas a certos momentos no passado geológico, logo o observação de todos os fatores na formação e evolução deste tipo específico de bacia sedimentar é dificultada.

Capítulo 3

Arcabouço Geológico da Bacia do Parnaíba

A Bacia do Parnaíba é uma das grandes bacias intracratônicas paleozoicas do Brasil, junto com as bacias do Paraná, Solimões e Amazonas. Sua área extende-se por 600 mil km^2 na porção Norte e Nordeste do Brasil, englobando os estados do Piauí, Maranhão, Tocantins, Pará, Ceará e Bahia. Em seu depocentro, é possível observar espessuras próximas de 3.500 metros de profundidade [Góes and Feijó, 1994, Vaz et al., 2007]. Regionalmente, a Bacia do Parnaíba é bordejada por blocos cratônicos e por faixas de dobramentos brasilianas [Cordani et al., 2009, de Castro et al., 2014]. Ao norte a bacia é limitada pelas bacias sedimentares da Margem Equatorial, o Cráton São Luís e pela Faixa Gurupi. Já a oeste, pela Faixa Araguaia e pelo Cráton Amazônico. Ao leste e sul, encontra-se o Cráton São Francisco e a Província Borborema, como pode ser visto na Figura 3.1.

3.1 Preenchimento Sedimentar

Góes [1995] aponta a dificuldade da compreensão do histórico deposicional da bacia junto com a compartimentação tectônica pré, sin e pós-ruptura do Macrocontinente Gondwana, devido a um preenchimento sedimentar com gênese, estilo tectônico e idade distinta. Com a dificuldade de relacionar todo esse registro sedimentar a uma única unidade geotectônica, sugeriu-se uma série de sub-bacias compondo uma grande província sedimentar, chamada Província Sedimentar do Meio-Norte. Já os trabalhos de Vaz et al. [2007], Daly et al. [2014], de Castro et al. [2016], Tozer et al. [2017] entendem que a Bacia do Parnaíba tem uma história deposicional marcada por 5 sequências tectônico-sedimentar primárias e dois pulsos magmáticos separados por discontinuidades geológicas regionais. O preenchimento sedimentar da bacia é caracterizado pelas

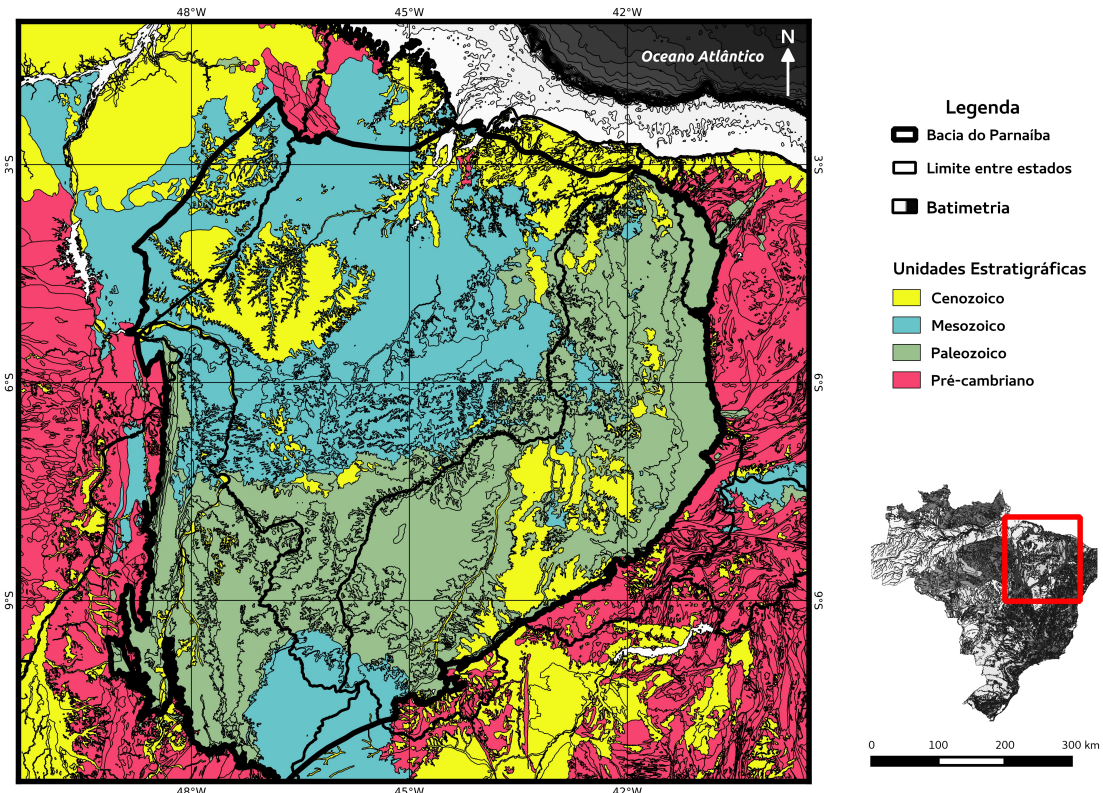


Figura 3.1: Mapa geológico da Bacia do Parnaíba.

sequências: Riachão, Jaibaras, Parnaíba, Mearim e Grajaú. Vaz et al. [2007] mostra que as sequências Riachão e Jaibaras formam um embasamento sedimentar da Bacia do Parnaíba. Porém existe uma diversidade de interpretações sobre a formação e idades dessas sequências sedimentar, principalmente para a sequência Richão, como é visto nos trabalhos de Castro et al. [2016] e Tozer et al. [2017]. As sequências iniciais são interpretadas como sedimentos pretéritos oriundos de eventos de riftamentos neoproterozóicos e cambro-ordovicianos, como mostra de Oliveira and Mohriak [2003] e de Castro et al. [2014]. A tectônica e idade dessas sequências ainda encontra-se em discussão nas pesquisas atuais, fato que não iremos abordar neste trabalho, pois não faz parte do escopo, mas pode ser observado nos trabalhos de Castro et al. [2014], Daly et al. [2014], de Castro et al. [2016], Tozer et al. [2017].

A tectono-sequência Parnaíba é relacionada a uma bacia cratônica do tipo sinéclise, denominada por Góes [1995] como a Bacia do Parnaíba, propriamente dita. Essa tectono-sequência tem idade entre o Ordoviciano Tardio até o incio do Triásico e consiste de três megasequências separadas por inconformidades regionais, como pode ser visto em Daly et al. [2014]. Estes depósitos são caracterizados por camadas

apresentando grande continuidade e espessuras regulares que se afinam progressivamente em direção às bordas da bacia, um comportamento característico do estilo de bacia do tipo sag. Os tipos de sedimentos associados a essa fase são marinhos rasos, fluvio-lacustre e siliciclásticos terrestres.

Vaz et al. [2007] mostra que a tectono-sequência Mearim, ou Jurássica, é composta apenas pela Formação Pastos Bons, que corresponde a depósitos lacustrinos com contribuição fluvial, em clima semi-árido a árido. A sequência é balizada na base e no topo por episódios magmáticos e é restrita apenas ao centro da bacia [Tozer et al., 2017]. Já a tectono-sequência Grajaú (Cretácea) é caracterizada por depósitos marinhos rasos, lacustres e flúvio-deltaicos, cuja deposição seria reflexo da abertura do Oceano Atlântico [Vaz et al., 2007]. Em afloramento, essa seqüência ocorre principalmente na porção noroeste-norte da bacia e sobrepõe-se discordantemente sobre as rochas das seqüências mais antigas. É importante frisar que o depocentro se deslocou durante a fase deposicional da bacia, com uma forte tendência para oeste, como mostra Tozer et al. [2017] através de dados de backstripping.

3.2 Magmatismo

A intensa atividade ígnea em que foram palcos as bacias do Parnaíba, Paraná, Amazonas e Solimões teve início com a abertura da Margem Equatorial durante a separação entre os continentes sul-americano e africano. Segundo Vaz et al. [2007] a Bacia do Parnaíba acomodou rochas ígneas intrusivas, diques e soleiras, e extrusivas de composição básica, as quais foram divididas em duas unidades: Formação Mosquito e Formação Sardinha. Essas formações são correlacionadas às rochas originadas a partir do rifteamento do supercontinente Pangea e da abertura do Oceano Atlântico, respectivamente. As idades isotópicas calculadas por Merle et al. [2011] apontam que a Formação Mosquito pertence à Província Magmática do Atlântico Central, já a formação Sardinha seria associada à Província Magmática Paraná-Etendeka.

Eventos precursores à desagregação do Gondwana Oeste propiciaram o abatimento da região central da bacia, com a formação de um sistema de riftes interiores, preenchidos pelos sedimentos das formações Pastos Bons e Corda associados ao alojamento das rochas básicas das formações Mosquito e Sardinha. A implantação desses riftes ocorreu, principalmente, sobre área da Estrutura de Xambioá, como mostra Mocitaiba et al. [2017]. As estruturas grabenformes geradas permitiram o alojamento desses eventos ígneos mesozoicos. Em subsuperfície, os diques da Formação Sardi-

nha e as soleiras da Formação Mosquito estão presentes em maior quantidade na tectono-sequência paleozoicas [Vaz et al., 2007].

3.3 Tectônica

A bacia do Parnaíba é circundada por inúmeras massas cratônicas arqueanas e por cinturões de dobramentos proterozoicos, como pode ser visto na Figura 3.1. Dois desses principais blocos formaram duas grandes massas continentais (São Francisco-Congo e São Luís-West Africa) que existiram antes da abertura do oceano Atlântico no mesozoico, e estavam envolvendo o bloco da Parnaíba, provável massa cratônica coberta pela bacia homônima. A existência desse bloco ocultado pela cobertura sedimentar foi postulada por inúmeras trabalhos nos ramos da geofísica, petrofísica, tectônica e geocronologia [Brito Neves et al., 1984, Cordani et al., 2009, Fuck et al., 2008, de Castro et al., 2014]. Análises de dados magnéticos e gravimétricos recentemente subdividiram esse bloco Parnaíba em pequenos fragmentos, denominados Parnaíba Norte, Parnaíba Sul e Teresina. Estes caracterizados pelas mudanças marcantes nas propriedades magnéticas e pelas variações de até 3.5 km na espessura crustal [de Castro et al., 2014].

No passado, estudos geofísicos da Bacia do Parnaíba delinearam uma grande quantidade de estruturas grabenformes abaixo da cobertura sedimentar, como mostra Brito Neves et al. [1984], Cordani et al. [2009]. Essas estruturas interpretadas foram utilizadas como suporte para modelos de subsidência termo-mecânicos, como o clássico modelo de McKenzie [1978]. Um refinamento mais recente deste conjunto de modelos foi proposto por de Castro et al. [2014], pela análise de anomalias gravimétricas e magnéticas. Os autores identificaram dois conjuntos de trends lineares no embasamento, o qual foram interpretados como dois estágios de riftamento, um relacionado ao fim da orogenia Brasiliiana e o outro precedendo a fase deposicional principal da bacia no Cambro-Ordoviciano. Em um grande perfil de reflexão sísmica profunda Daly et al. [2014] não encontrou evidência de uma fase de riftamento neoproterozóica postulada previamente, e notou uma inconformidade subplanar cortando todos os blocos crustais interpretados no perfil, Borborema, Parnaíba e Amazônico. Segundo os autores, os limites principais e as estruturas do embasamento não teriam uma grande influência na formação da bacia e propõem que uma subsidência termal se tornaria um provável mecanismo para a formação e evolução da bacia do Parnaíba.

A viabilidade de um modelo de riftamento para a bacia foi investigada exaustivamente por Tozer et al. [2017] através dos estudos das anomalias Bouger desenvolvidas

em cima do mesmo perfil sísmico de Daly et al. [2014], backstripping dos dados de poços disponíveis e da modelagem sísmica de uma rede densa de receptores no centro da transecta. O estudo demonstrou que o modelo de riftamento não é capaz de explicar as estruturas crustais inferidas, assim como a história de subsidência dessa bacia. Devido a grande quantidade de intrusões magmáticas na bacia, os autores postularam existência de uma grande corpo máfico de 12-20 km de espessura na crosta inferior que serviria como um carga que causaria uma subsidência flexural. Através da relaxão do esforço viscoelástico essa carga poderia explicar a longa história de subsidência observada nos registros de poços. No entanto, os autores não restringem os limites dessa carga em profundidade e ainda não existem evidências geológicas de um magmatismo extensivo no início da bacia, prova cabal para poder afirmar esse corpo magmático na crosta inferior.

Capítulo 4

Artigo: Deep crustal architecture of the Parnaíba basin of NE Brazil from receiver function analysis: Implications for basin subsidence

O artigo intitulado: "*Deep crustal architecture of the Parnaíba basin of NE Brazil from receiver function analysis: Implications for basin subsidence*" foi submetido para a The Geological Society Special Publications e passa pela segunda revisão no momento. Este artigo corresponde a estimativas pontuais de espessura crustal e razão Vp/Vs em 9 estações numa transecta NW-SE na parte central da bacia, junto com perfis de velocidade de onda S obtidos na inversão conjunta entre funções do receptor e velocidades de ondas de superfície.

1 Deep crustal architecture of the Parnaíba basin of
2 NE Brazil from receiver function analysis:
3 Implications for basin subsidence.

4 Diogo L.O. Coelho^{1,*}, Jordi Julià^{1,2}, Verónica Rodríguez-Tribaldos³, Nicholas
5 White³

6 ¹*Programa de Pós-graduação em Geodinâmica e Geofísica, Universidade Federal do Rio
7 Grande do Norte, Lagoa Nova, Natal-RN, CEP 59078-970, Brazil*

8 ²*Departamento de Geofísica, Universidade Federal do Rio Grande do Norte, Lagoa Nova,
9 Natal-RN, CEP 59078-970, Brazil*

10 ³*Bullard Laboratories, Department of Earth Sciences, University of Cambridge, Madingley
11 Rise House, Madingley Road, Cambridge, CB3 0EZ, UK*

12 *Corresponding author (e-mail: locdiogo@gmail.com)

13 **Abstract**

14 We investigate the crustal architecture of the Parnaíba basin of NE Brazil by analyzing
15 receiver functions along a ~600 km-long transect crossing the central portion of the basin.
16 The transect consisted of 9 broadband stations interspaced at ~70 km distance and record-
17 ing continuously for a period of 15 months, with the goal of improving our understanding of
18 the origin and evolution of this large cratonic basin. Our results reveal that crustal thickness
19 varies between 39 and 45 km along the transect, gradually thickening towards the depocen-
20 ter, and that bulk Vp/Vs ratios vary between 1.70 and 1.78. The crust can be generally
21 divided into a 2.0-3.5 km thick layer of low-velocity sediments, a 15-20 km thick upper crust
22 with S-velocities around 3.5-3.6 km/s, and a 18-22 km thick lower crust with S-velocities
23 around 3.7-3.8 km/s. Near the depocenter, where the crust is thickest, the bottom 10-12

24 km of the crust are characterized by fast S-velocities around 4.0-4.2 km/s. The crust-mantle
25 boundary is generally gradational, and reaches typical upper mantle S-velocities of 4.5-4.6
26 km/s. Our findings confirm that stretching of the lithosphere must be minimal - as indepen-
27 dently suggested by seismic profiling, gravity modeling, and surface geology - and are found
28 compatible with models invoking flexural subsidence driven by a deep, buried load. However,
29 loading from a thick, high-density layer of mafic intrusives pervading the lower crust - as re-
30 cently proposed for the basin - is found inconsistent with bulk Vp/Vs ratios and lower crustal
31 velocities from our S-velocity models. Flexural bending by a deeper load, perhaps related
32 to convecting processes in the underlying asthenosphere, seems more plausible, but need to
33 be investigated further in order to fully assess the origin and evolution of the Parnaíba basin.

34

35 **Keywords:** Cratonic subsidence, Basement architecture, South America

36

37 Introduction

38 The genesis and evolution of large basins in the stable interiors of continents is an impor-
39 tant geological problem that is not easily understood within the Plate Tectonics paradigm.
40 In spite of notable attempts by *Klein and Hsui (1987)* to link the formation of all cratonic
41 basins of Europe, Africa, North and South America to rifting and break-up of a Late Pre-
42 cambrian supercontinent, no single mechanism seems capable of explaining the development
43 of cratonic basins on such a large scale. This inability is nicely illustrated in *Kaminski and*
44 *Jaupart (2000)*, who showed that in spite of the four major cratonic basins of North America
45 - Hudson Bay, Michigan, Illinois, and Williston - having similar ages and being close to one
46 another, they exhibit different subsidence histories and are characterized by different time-

47 scales and sediment thicknesses. Adding to this complexity, is the intriguing observation
48 that prolonged intervals of slow subsidence alternate with fast subsidence rates (*Cloetingh*
49 *and Burrov, 2011*). Although periods of fast subsidence often coincide with orogenic activity
50 at plate boundaries, the impression remains that individual mechanisms might be needed
51 to understand the large variety of depositional histories in cratonic basins worldwide.

52 The Parnaíba basin of NE Brazil is one of three large Paleozoic basins in stable South
53 America - together with the Paraná basin of SE Brazil and the Amazon basin, in the northern
54 half of the continent. The basin is commonly described as a large, sag-type cratonic basin,
55 with a roughly circular shape and a depocenter reaching up to 3.5 km depth (*Góes and Feijó,*
56 *1994; Vaz et al., 2007; Daly et al., 2014*). It is generally agreed that initial subsidence of the
57 basin occurred in an intra-continental setting during Paleozoic times, with the proto-basin
58 being framed by three large cratonic masses (Figure 1): Amazon to the West, São Luiz-West
59 Africa to the North, and São Francisco-Congo to the South and East (*Almeida et al., 1981;*
60 *Brito Neves et al., 1984; Cordani et al., 2009; Brito Neves and Fuck, 2013; Cordani et al.,*
61 *2013*). The physical mechanism behind its subsidence and evolution, on the other hand,
62 is more controversial. A number of basin-forming mechanisms have been proposed for this
63 basin, which fall into one of the following broad categories: (i) Thermally-driven subsidence,
64 which is based on a number of seismically identified unconformities in the sedimentary record
65 of the basin combined with evidence lacking for rifting structures (*Daly et al., 2014*); (ii)
66 thermo-mechanical subsidence, which relies on the inference of graben-like structures in the
67 basin's basement from interpreted gravity, magnetic, and pseudo-gravity residual anomalies
68 (*Brito Neves et al., 1984; Nunes, 1993; Cordani et al., 1984; de Castro et al., 2014*); and
69 (iii) flexural subsidence, driven by the load of a high-density, intrusive body in the lower
70 crust, postulated from modeling of gravity anomalies (*Tozer et al., 2017*).

Very little is known about the deep, crustal architecture of this enigmatic cratonic basin. Most of our current knowledge is restricted to low-resolution, continental-scale studies (*Feng et al., 2004; 2007; Lloyd et al., 2010; van der Meijde et al., 2013; Assumpção et al, 2013a; 2013b; Uieda and Barbosa, 2017*), a single seismic reflection line crossing the basin in the EW direction (*Daly et al., 2014*), and a colocated gravity survey along the same EW-trending line (*Tozer et al., 2017*). Continental-scale studies showed the crust is thinnest (30-35 km) under the Proterozoic provinces of South America, while thickest under cratonic landmasses (e.g. Amazon and São Francisco, 41 ± 4 km) and cratonic basins (e.g. Paraná and Parnaíba, 42 ± 4 km). More detailed information was developed from the seismic reflection survey of *Daly et al. (2014)*, where a basin-wide migrated cross-section demonstrated the presence of up to three different crustal blocks under the basin: a 35-44 km thick, highly reflective crustal block to the East, interpreted as the continuation of the Proterozoic Borborema Province; a ~ 40 km thick, moderately reflective crustal block to the West, identified as the Amazon craton; and a central, almost transparent crustal block referred to as the Parnaíba block with a locally defined Moho at about 38 km depth. Surprisingly, no crustal thickness estimates were reported for most of the central Parnaíba block, as the reflection signature expected from the crust-mantle boundary seemed to be absent in the migrated cross section. Most recently, seismic and gravity modeling along a profile coincident with the seismic reflection line has revealed a two-layer crust for the Parnaíba block, with an upper-lower crustal boundary at 17-25 km depth and a relatively flat Moho at $\sim 42 \pm 2$ km depth (*Tozer et al., 2017*).

In this work, we characterize the deep, crustal architecture of the Parnaíba basin by mapping subsurface seismic discontinuities with teleseismic P-wave receiver functions (*Langston, 1979*). We present point estimates of crustal thickness and Vp/Vs ratio at 9 broadband sta-

tions developed through the $H\kappa$ -stacking procedure of *Zhu and Kanamori (2000)*, along with detailed S-wave velocity-depth profiles obtained from the joint inversion of receiver functions and surface-wave dispersion velocities (*Julià et al., 2000; 2003*). The $H\kappa$ -stacking analysis reveals the crust could be as thick as 44-45 km around the basin's depocenter and that it progressively thins to 39-41 km towards the edges, while bulk V_p/V_s ratios are in the 1.70-1.78 range along the transect, with larger values around the depocenter. The velocity-depth profiles confirm crustal thickness variations from the $H\kappa$ -stacking analysis and additionally reveal a lower crustal layer below 18-22 km depth, with S-velocities in the 3.7-3.8 km/s range that locally raise to 4.0-4.2 km/s near the depocenter. Our findings favor models invoking minimal stretching of the basin's underlying crust and are found compatible with flexural bending by a deep load. However, the existence of a thick, intrusive body pervading the lower crust is not supported by our results. We argue that deep convecting processes in the asthenosphere might provide an alternative loading mechanism.

Geology and Tectonic Setting

The depositional history of the Parnaíba basin is built on five primary tectono-sedimentary sequences and two magmatic pulses separated by regional unconformities (*Góes and Feijó, 1994; Vaz et al., 2007*). Following *Tozer et al. (2017)*, the basin infill is characterized by five distinct tectonostratigraphic sequences: Riachão, Jaibaras, Parnaíba, Mearim, and Grajau, separated by basin-wide unconformities. The first two sequences have been traditionally interpreted as infills resulting from Neoproterozoic (*de Castro et al., 2014*) and Cambro-Ordovician (*Oliveira and Mohriak, 2003*) rifting events, respectively, but other interpretations exist (see *Tozer et al., 2017*). The Parnaíba sequence has been attributed to cratonic subsidence, and is arranged into three megasequences also separated by regional

118 unconformities and ranging in age from Late Ordovician to Early Triassic (e.g. *Daly et al.*,
119 *2014; de Castro et al., 2014; Tozer et al., 2017*). Two magmatic events of Early Jurassic and
120 Early Cretaceous ages - expressed in the Mosquito and Sardinha formations, respectively
121 - are observed within the basin. The Mosquito Formation represents a phase of extrusive
122 volcanism related to the Central Atlantic Magmatic Province (*e.g. Góes et al., 2003*) that
123 seals the Parnaíba stratigraphy, and is overlain by the Late Jurassic Mearim sequence in the
124 center of the basin. The Sardinha Formation manifests itself as sills interfingering with basin
125 strata, and has been related to the early opening of the South Atlantic Ocean (*Merle et al.*
126 *(2011)*). The youngest sequence overlies the Parnaíba and Mearim units unconformably to
127 the North. It was deposited during Cretaceous times - likely due to processes related to the
128 opening of the South Atlantic (*e.g. Rossetti et al., 2004*) - to form the Grajau subbasin.
129 Alluvial and aeolian deposits of Cenozoic age cover large areas of the Parnaíba basin (see
130 Figure 1).

131 The Parnaíba basin is framed by the Amazonian craton to the West, the São Francisco
132 craton to the Southeast, the São Luiz craton to the North, and the Proterozoic Borborema
133 Province to the East (Fig. 1). Two of these major cratonic blocks were part of larger cra-
134 tonic landmasses (São Francisco-Congo and São Luiz-West Africa) that existed before the
135 opening of the Atlantic ocean in Mesozoic times, and likely surrounded a central Parnaíba
136 block presently concealed under the basin's sediments. The existence of a Parnaíba block
137 was postulated from geophysical evidence, petrography, and Rb-Sr and K-Ar geochronology
138 of basement rocks (*Cordani et al., 1984*), as well as from collisional tectonic models (*Brito*
139 *Neves et al., 1984; Klein et al., 2008; Nunes, 1993*), and it was regarded as one of the
140 continental fragments inherited by the South American platform after the dispersal of the
141 Rodinia supercontinent (*Fuck et al., 2008*). Analysis of recent airborne magnetic and grav-

142 ity surveys further subdivide the Parnaíba block into smaller fragments - Parnaíba North,
143 Parnaíba South, and Teresina - characterized by marked changes in magnetic properties and
144 by variations of up to 3.5 km in crustal thickness (*de Castro et al., 2014*).

145 Early geophysical studies of the Parnaíba basin, mostly based on data collected during
146 magnetic and/or gravity surveys, delineated a number of graben-like structures concealed un-
147 der the basin's sediments (e.g. *Brito Neves et al., 1984; Nunes, 1993; Cordani et al., 1984*).
148 These interpreted structures were then utilized to support models of thermo-mechanical
149 subsidence for the basin, mostly following the classical model of *McKenzie* (1978). A most
150 recent refinement of this set of models was proposed by *de Castro et al. (2014)*, from analysis
151 of airborne magnetic and gravimetric anomalies. The authors identified two sets of linear
152 trends in the basement, which were interpreted as two separate rifting stages - an older
153 one at the end of the Brasiliano orogeny and a younger one in the Cambro-Ordovician -
154 preceding major sag deposition. Interestingly, *Daly et al. (2014)* found no evidence of the
155 early Neoproterozoic phase of rifting postulated by *de Castro et al. (2014)* in their seismic
156 reflection line, and noted that the marked, subplanar unconformity imaged at the base of the
157 Phanerozoic section crossing all three crustal blocks (Borborema, Parnaíba and Amazonian)
158 might represent a major peneplanation surface. They argued that the major boundaries and
159 associated basement structures would have little to do with the formation of the basin and
160 - as the peneplain surface must postdate the complexity of the basement below - thermal
161 subsidence would become a more likely driving mechanism for the formation and evolution
162 of the Parnaíba basin.

163 The viability of the rifting model for the Parnaíba basin was extensively investigated in
164 *Tozer et al. (2017)* from modeling of Bouguer anomalies developed along the same seismic
165 transect of *Daly et al. (2014)*, backstripping of available well data, and modeling of a

166 densified seismic survey in the center of the transect. The study demonstrated - quite
167 convincingly - that a rifting model is unlikely to be able to explain the inferred crustal
168 structure and subsidence history of this basin, and postulated the existence of a 12-20 km
169 thick, lower crustal body pervading the Parnaíba block. The authors suggested that this
170 body would have resulted from magmatic intrusion of the lower crust and that it would be
171 acting as a buried load causing flexure of the basin's surface. They further argue that such
172 a model could explain, through viscoelastic stress relaxation, the long subsidence history
173 recorded in the deep wells along with the stratigraphic offlap that is well documented in at
174 the eastern edge of the basin. However, the authors caution that precise constraints on the
175 vertical emplacement of the buried load are lacking, and that geologic evidence of extensive
176 magmatism at the time of basin initiation - as expected from the large size of the postulated
177 magmatic body in the lower crust - is missing.

178 Data and data processing

179 The dataset utilized in this work was acquired by the Universidade Federal do Rio
180 Grande do Norte and the University of Cambridge as part of the broader Parnaíba Basin
181 Analysis Project (PBAP), a multi-disciplinary effort funded by BP Energy do Brasil that
182 aims at improving our current knowledge of the origin and evolution of this large cratonic
183 basin. The dataset was collected at 9 seismic stations deployed along an approximately EW
184 trending line superimposed to the seismic reflection line of *Daly et al. (2014)*. The stations
185 were interspaced at distances of 50-70 km, covering a total length of ~600 km in the central
186 portion of the basin (see Figure 1). A total of 8 seismic stations were equipped with three-
187 component, Nanometrics Meridian Compact Posthole sensors, with a frequency response flat
188 in velocity between 120 s to 108 Hz, and integrated high-gain digitizers. One station, located

189 in the center of the linear deployment, was equipped with a three-component, Güralp GMT-
190 3T sensor, also with flat response in velocity down to 120 s, and feeding a DM24 digitizer.
191 All stations operated continuously sampling at 100 samples per second and resorted to GPS
192 signal for timekeeping. The central station - contributed by the University of Cambridge -
193 was deployed in August, 2015, while the remaining broadband stations started operations
194 in March, 2016. Location coordinates and recording time windows considered for analysis
195 in this work are listed in Table 1.

196 In order to develop receiver function estimates for each of the 9 seismic stations in the
197 deployment, seismic sources with epicentral distances between 30° and 90° and magnitudes
198 above 5.5 mb were considered. Receiver functions are obtained by deconvolving the vertical
199 component of the teleseismic P-coda from the corresponding radial component, which effec-
200 tively removes the signature of the source and instrument response, and leaves the signature
201 of secondary P-to-S converted waves created at seismic discontinuities under the receiver
202 (*Langston, 1979; Ammon, 1991*). Analysis of the amplitudes and travel-times in the re-
203 ceiver functions can then be utilized to develop constraints on the seismic structure under
204 the station (*Owens et al., 1984; Ammon et al., 1990*). Moreover, the deconvolution process
205 equalizes the teleseismic waveforms, which can be stacked to produce high signal-to-noise
206 ratio estimates of the receiver response under a seismic station. The deconvolution proce-
207 dure can also be applied to the transverse component of the teleseismic P-wave coda. The
208 transverse component should be identically zero for isotropic, laterally homogenous propa-
209 gating media, so the observation of P-to-S conversions in the transverse receiver function is
210 usually diagnostic for dipping or anisotropic structures under the station (*Savage, 1998*).

211 To effectively compute receiver function estimates, the selected seismograms were cut
212 10 s before and 120 s after the P-wave arrival, demeaned, detrended, tapered with a 5%

213 cosine window, and band-pass filtered between 0.05 Hz and 4 Hz. The high-pass corner
214 frequency was selected to remove low-frequency noise from the recorded waveforms, while
215 the low-pass corner frequency was chosen to avoid aliasing before re-sampling to 10 samples
216 per second. The decimated waveforms were next rotated into the great-circle-path to obtain
217 the radial and transverse components of ground motion, and low-pass filtered with acausal
218 Gaussian filters of widths 1.0 ($f < \sim 0.5$ Hz) and 2.5 ($f < \sim 1.25$ Hz). The filtered verti-
219 cal component was then deconvolved from the corresponding filtered horizontal (radial and
220 transverse) components through the time-domain, iterative scheme of *Ligorría and Ammon*
221 (1999), with 500 iterations. The deconvolved time series were finally low-pass filtered with
222 the same Gaussian filters of widths 1.0 and 2.5 to produce low- and high-frequency receiver
223 function estimates, respectively. A strict quality control was applied to the deconvolved
224 waveforms. First, the radial receiver function was convolved back with the correspond-
225 ing vertical component to reconstruct the radial component, and those receiver functions
226 not reproducing at least 85% of the original radial component were removed. Second, the
227 transverse receiver functions were visually examined and the radial receiver functions associ-
228 ated to those exhibiting anomalously large amplitudes were excluded from further analysis.
229 Third, the remaining radial receiver functions were visually inspected for outliers, which
230 were also excluded from further analysis. A total of 165 low-frequency receiver functions
231 and 189 high-frequency receiver functions, out of 4129 waveforms selected for processing,
232 passed our quality control.

233 Average radial and transverse high-frequency receiver functions for each of the 9 stations
234 considered in this study are displayed in Figure 2. The receiver function waveforms have
235 been averaged within groups that do not exceed $\pm 5^\circ$ in back-azimuth and ± 0.05 s/km in
236 ray parameter. A close inspection of the waveforms reveals important properties about the

propagating medium. For instance, the first 3-4 s of the receiver functions are dominated by the signature of the sedimentary cover. Note that the main peak is displaced with respect to the zero lag time, which is the combined effect of a small direct P-wave followed by a large Ps conversion at the sediment-bedrock interface (see e.g. *Zelt and Ellis, 1998*). The peak and trough trailing the displaced large amplitude, at lag times around 2-3 s, are likely to be multiply reverberated phases between the surface and the sediment-bedrock interface. Luckily, the seismic energy reverberating in the sedimentary layer does not mask the signature of P-to-S conversions from deeper discontinuities. The peak at about 5 s lag time observed in most of the waveforms is consistent with a Ps conversion at the crust-mantle boundary, and the peak at about 15 s lag time is consistent with the first reverberation (PpPs phase) in the crust. The second multiple is generally harder to identify, but it can be observed at about 20 s lag time in some waveforms. The transverse components display amplitudes that are generally small when compared to the corresponding radial components, indicating that lateral variations in earth structure are small and that the medium under the stations can be regarded as laterally homogeneous. The only exception is station BDCO, for which large transverse amplitudes with opposite polarity near zero lag time suggest the presence of a strongly dipping, near-surface interface (see e.g. *Savage, 1998*).

Crustal Architecture

Crustal thickness and bulk Vp/Vs ratio

Crustal thickness and bulk Vp/Vs ratio can be estimated from receiver functions utilizing the H- κ stacking approach of *Zhu and Kanamori (2000)*. This procedure performs a grid-search over a stacking surface that is built by summing a weighted combination of Ps, PpPs

and PpSs+PsPs amplitudes from individual receiver functions. The Ps phase denotes a P-to-S conversion upon refraction across the Moho, while the PpPs and the PpSs+PsPs phases denotes multiple reverberations between the free surface and the Moho containing two P-wave and one S-wave segments and one P-wave and two S-wave segments, respectively (see e.g. *Ammon, 1991*). The summation is performed along the corresponding phase-moveout curves for the three phases, which are computed after assuming a simple layer-over-half space model for the receiving structure. During the calculation, the P-velocity for the layer has to be specified *a priori*, while the thickness and Vp/Vs ratio are left as free parameters.

The summation of amplitudes is performed according to

$$s(H, \kappa) = w_1 \times r(t_1) + w_2 \times r(t_2) - w_3 \times r(t_3) \quad (1)$$

where $r(t)$ is the radial receiver function, t_1 , t_2 and t_3 are the predicted Ps, PpPs, and PsPs+PpSs arrival times for the crustal thickness H and Vp/Vs ratio κ , and the w_i are *a priori* weighting factors. Crustal thickness and Vp/Vs ratios are varied within prescribed ranges, and the maximum in the H- κ stacking surface is taken as an estimation of crustal thickness and bulk Vp/Vs ratio under the station.

Examples illustrating the performance of the H- κ stacking procedure to select stations in the Parnaíba basin are given in Figure 3. Note the analysis was always applied to high-frequency receiver functions to obtain the best resolution possible. The figures display the H- κ stacking surface on top and the receiver function waveforms, sorted by ray parameter, at the bottom. In both cases a single local maximum is observed on the H- κ stacking surface, displaying crustal thicknesses of 40.0 ± 0.4 km and 43.6 ± 0.7 km and Vp/Vs ratios of 1.70 ± 0.01 and 1.78 ± 0.03 for stations STSR and GRJU, respectively. Confidence bounds

were obtained after bootstrapping the receiver function dataset with 200 replications (*Efron and Tibshirani, 1991*). Note that, due to additional uncertainty in the assumed P-wave velocity, formal confidence bounds must be increased by ± 1 km for crustal thickness and ± 0.01 for Vp/Vs ratio (see Table 2). At station STSR, the receiver function waveforms display well-defined peaks at around 5, 16, and 20 s, which the algorithm picks as the Ps, PpPs and PpSs+PsPs phases, respectively. At station GRJU, on the other hand, the waveforms display well-defined peaks at around 5.5, 18, and 22 s for the Ps and crustal multiples, resulting in a thicker crust with larger Vp/Vs ratio.

For two of the sites, stations BPPF and GENI, we could not obtain reliable results from the H- κ stacking analysis. Lateral variations in velocity structure around these two stations might be generating inconsistent P-to-S conversions that do not stack coherently when combined all together. This was investigated by grouping the corresponding receiver functions by back-azimuth (recall Figure 2) and running the H- κ stacking separately within each group. For station BPPF, we obtained a crustal thickness of 45.8 ± 0.2 km for sources located at 166° and 42.7 ± 1.5 km for sources located at 294° , with Vp/Vs ratios of 1.73 ± 0.02 and 1.74 ± 0.03 , respectively; for station GENI, we obtained a crustal thickness of 45.1 ± 0.9 km at 293° , with a Vp/Vs ratio of 1.77 ± 0.03 . In both cases, there are back-azimuths for which the H- κ stacking did not yield any results.

A summary of crustal thicknesses and bulk Vp/Vs ratios for the broadband stations sampling the Parnaíba basin is given in Table 2. In general, we assigned weights of 0.4, 0.3, and 0.3 to the Ps, PpPs and PpSs+PsPs phases when they were clearly observed in the receiver function waveforms; however, when one of the multiples was not clearly observed, we assigned a weight of 0.0 to that phase and weights of 0.5 to the remaining phases. As no independent estimates of P-velocity exist for the basin, we opted to base our calculations on

the worldwide average of 6.5 km/s derived for continental crust from crustal compilations (*Christensen and Mooney, 1995*) and assess variations in the inferred crustal values for P-velocities varying between 6.3 and 6.7 km/s. The results in Table 2 reveal that crustal thicknesses range between 39 and 46 km and have combined confidence bounds of ± 2 km, if we assume uncertainties in P-velocity of ± 0.1 km/s. Vp/Vs ratios are more variable and less well-constrained, although most of the measurements range between 1.69 and 1.76 and have combined confidence bounds below ± 0.08 . Note that, for Vp/Vs ratios, uncertainties due to variation in P-velocity are significantly smaller than those obtained from bootstrapping the dataset. The resulting variation in crustal thickness along the deployment is further illustrated in Figure 4. The figure reveals the crust thickens from 40-42 km at the edges to 43-46 km near the depocenter (stations GRJU, GENI and BDCO), and that this thickening is accompanied by an increase in Vp/Vs ratio from 1.70-1.72 at the edges to 1.77-1.78 near the depocenter. This trend in Vp/Vs is somehow disrupted by station PRDT, but the confidence bounds are large and can be accommodated.

319 S-wave velocity-depth profiles

320 S-wave velocity-depth profiles for each individual station along the transect were developed by inverting the receiver function waveforms in this study jointly with independent 321 surface-wave dispersion velocities. We followed the approach of *Julia et al. (2000; 2003)*, in 322 which a linear combination of the root-mean-square error for both datasets and a roughness 323 norm for the velocity model are minimized through a linearized, iterative inversion scheme. 324 In that approach, the datasets are equalized for the different number of data points and 325 physical units through normalization by $N\sigma^2$, where N is the number of data points and σ^2 326 is the data variance, and pre-multiplied by an influence factor ($0 < p < 1$) that controls 327

328 the relative contribution of each data set to the total norm. Following previous studies (e.g.
329 *Julia et al., 2003; 2008*), we considered an influence factor of 0.5 - giving equal importance
330 to each data set - and average variances of 0.0001 s^{-2} and 0.0025 (km/s)^2 for the receiver
331 functions and dispersion velocities, respectively. In general, 6 iterations sufficed to achieve
332 convergence.

333 The starting model adopted during the inversion consisted of a perfectly elastic, laterally
334 homogeneous and isotropic medium defined through a stack of thin layers of fixed thickness
335 and uniform velocity. The crust has a linear velocity increase from 3.4 km/s at the surface
336 to 4.0 km/s at 42.5 km depth and overlies a 4.5 km/s upper mantle. The top two layers are
337 1.0-2.0 km thick, with thicknesses carefully chosen for each station to precisely match P-to-
338 S amplitudes from the sediment-bedrock interface in the first 3-4 s of the receiver function
339 waveforms. This forward modeling exercise was important, as we observed uppermost crustal
340 velocities may trade-off with sedimentary structure. Layer thicknesses then progressively
341 increase from 2.5 km at crustal levels to 5 km in the lithospheric mantle and to 10 km down
342 to 220 km depth, thus reflecting the decrease in resolution with depth associated to the
343 datasets (see e.g. *Julia et al., 2003*). As dispersion velocities have partial sensitivity to
344 deep mantle structure at long periods, the starting model is further parameterized down to
345 ~ 500 km depth with flattened PREM velocities (*Dziewonski and Anderson, 1981*), which
346 are constrained to remain unchanged during successive iterations. A flattened PREM might
347 not be the actual structure in the deep mantle under the Parnaíba basin, but will suffice to
348 account for the partial sensitivity of dispersion velocities (see *Julia et al., 2003*).

349 Dispersion velocities were borrowed from the continental-scale, surface-wave tomography
350 study of *Feng et al. (2004)*. In that study, local group-velocity dispersion curves for the
351 fundamental-mode of Rayleigh-waves were developed for periods between 10 and 140 s for the

352 South American continent. Single-station measurements at broadband stations widespread
353 throughout the continent were first taken on the vertical component of regional seismograms
354 collected between 1990 and 2003, with sources located mainly along plate boundaries. This
355 resulted in over 6,000 single-station dispersion curves that were then tomographically in-
356 verted to develop local dispersion curves within cells that formed a $1^\circ \times 1^\circ$ grid covering the
357 entire continent. Although not reported in the study, uncertainties were estimated to range
358 from ± 0.05 km/s at short periods to ± 0.12 km/s at longer periods (M. Assumpção, pers.
359 comm., 2008). The velocity-depth profiles presented in our study were thus developed by
360 jointly inverting the receiver functions at a given station with the local dispersion curve
361 associated to the tomographic cell enclosing that station.

362 The performance of the joint inversion procedure is illustrated in Figure 5 through sta-
363 tions STSR and GRJU, which are located on opposite sides of the transect. The figure
364 displays the starting and final joint inversion models, along with the fits between observed
365 and predicted receiver functions and Rayleigh-wave dispersion curves for each station. Note
366 that the receiver function dataset includes all the averages at high- and low-frequency con-
367 tents developed for a given station (recall Figure 2). The match between observations and
368 predictions is excellent in both cases, with the fine layering introduced at the top of the
369 model successfully accounting for observed variations in receiver function amplitudes during
370 the first 3-4 seconds in the waveforms. For station STSR, the inverted velocity-depth profiles
371 is simple, and reveals a ~ 38.0 km thick crust with a smooth velocity increase with depth,
372 an upper crust of ~ 3.5 km/s down to ~ 18 km depth, and a lower crust varying between
373 3.6 and 3.9 km/s down to Moho depths; for station GRJU, the crust is 41-43 km thick and
374 displays a 3.5-3.6 km/s upper crust down to ~ 19 km depth overlying a 3.7-3.8 km/s lower
375 crust down to Moho depths. Sediment thicknesses are 2.0 km for station STSR and 3.5 km

376 for station GRJU. The crust-mantle boundary is modeled as a sharp discontinuity under
377 station STSR, and as a gradational transition under station GRJU, as expected from the
378 comparatively small amplitudes displayed by the crustal multiples in comparison to the Ps
379 phase (e.g. *Julia*, 2007). Upper mantle velocities are around 4.5-4.6 km/s for both stations.

380 Confidence bounds for the S-velocity model at a given station were developed after
381 jointly inverting high- and low-frequency receiver functions within each group with the
382 dispersion curve for that seismic station. This resulted in the development of several velocity
383 models for each station (i.e. 4 at station STSR and 5 at station GRJU), which were then
384 utilized to compute the standard deviation in S-velocity for each layer with respect to the
385 "average" velocity model (i.e. the model from the joint inversion of all receiver function
386 groups and the dispersion curve). Confidence bounds were reported as grey bands around
387 the "average" velocity model, marking the 2σ -variation in S-velocity for each layer. Figure 5
388 shows that confidence bounds are ± 0.1 km/s down to 80-90 km depth and may grow to ± 0.2
389 km/s at larger depths, although they may locally grow bigger if lateral variations in earth
390 structure around the station are required to match features unique to a particular receiver
391 function group. Given the parameterization of our models, uncertainties in the depth of the
392 discontinuities are at least one layer thickness, this is, ± 2.5 km.

393 A summary of the S-velocity models developed for the stations in the Parnaíba basin is
394 displayed in Figure 6. Within confidence bounds, the velocity-depth profiles corroborate the
395 results from the H- κ stacking analysis and reveal a thickening of the crust around station
396 GENI, near the basin's depocenter. The profiles also show the crust is generally structured
397 in two layers: (i) a 15-20 km thick upper crust with S-velocities around 3.5-3.6 km/s, and (ii)
398 a 18-22 km thick lower crust with S-velocities around 3.7-3.8 km/s. However, under station
399 GENI - where the crust is thickest - the bottom 10-12 km of the crust are characterized by

400 faster velocities of 4.0-4.2 km/s. Such a high-velocity lower crust is not observed under the
401 other stations. In the upper mantle, velocities are 4.5-4.6 km/s immediately below the Moho
402 and slowly increase to faster values with depth. The sediment-bedrock interface is located
403 at 1.5-3.5 km depth, thickening towards the depocenter, and sediments display velocities in
404 the 1.7-2.4 km/s range. The figure also superimposes the depths of the main crustal features
405 outlined in the crustal model of *Tozer et al.* (2017) from analysis of seismic reflection and
406 gravity data. Crustal thicknesses are generally similar, but the receiver function models
407 require a thickening under stations GRJU, GENI, and BDCO, and a slight thinning under
408 stations STSR and BUCO, that does not seem to be required in their model. Similarly, an
409 upper-lower crust interface is observed in both the gravity and receiver function models at
410 similar depth ranges, but the respective topographies do not precisely match. The agreement
411 for the sediment-bedrock interface is remarkable, considering the simple forward-modeling
412 approach utilized in the receiver function modeling.

413 Implications for basin subsidence

414 The results on crustal thickness and velocities reported in the previous section have re-
415 vealed that the crust thickens from 39-42 km at the edges to 43-45 km near the depocenter,
416 and that the thickening is accompanied by: (i) an increase in Vp/Vs ratio from 1.70-1.75 to
417 1.77-1.78, and (ii) by a layer of fast-velocity material of 4.0-4.2 km/s at the bottom of the
418 crust. Our crustal thicknesses are thus at odds with models of basin evolution that invoke
419 initial mechanical stretching of the basin's lithosphere. According to global compilations
420 (e.g. *Durrheim and Mooney, 1991; Zandt and Ammon, 1995*), the crust of Precambrian
421 terrains worldwide is between 35 and 45 km thick. A crustal thickness range of 39-45 km for
422 the Parnaíba block can therefore be regarded as average. Moreover, an average crustal thick-

ness indicates that if mechanical stretching occurred before subsidence, the corresponding stretching factor was small. Small stretching factors imply minimal subsidence from initial mechanical stretching and from subsequent cooling of the advected asthenosphere (*McKenzie, 1978*). Thus, a crustal thickness range of 39-45 km, consistent with crustal thickness of outcropping Precambrian terrains worldwide, indicates that mechanical stretching of the Parnaíba basin - if it existed at all - did not play a significant role during its formation and further evolution.

Our results do not support either a pervasive body of magmatic intrusives making the lower crust of the Parnaíba block, as suggested in *Tozer et al. (2017)*. Laboratory measurements in rock samples show that typical Vp/Vs ratios for mafic lower crustal lithologies - i.e. mafic granulite and mafic garnet granulite - are around 1.81 - 1.82 (*Christensen, 1996*), so a mafic lower crust should increase the bulk Vp/Vs ratio for the entire crustal column. Back-of-the-envelope calculations show that a bulk Vp/Vs ratio of 1.76 is compatible with the presence of a layer of 5-6 km of mafic material in the lower crust (see *Luz et al., 2015*); a thicker layer, however, should increase the bulk Vp/Vs ratio above 1.76. Our bulk Vp/Vs ratios range between 1.70 and 1.75 along the edges of the profile, and grow to 1.77-1.78 near the depocenter, which suggests that magmatic intrusives are restricted to the region where the crust is thickest. Moreover, using a P-velocity range of 7.0 - 7.6 km/s for mafic lower crustal material (*Durrhem and Mooney, 1991*) and the Vp/Vs ratios of *Christensen (1996)*, we conclude that S-velocities in the 3.9 - 4.2 km/s range may correspond to mafic rocks. Only the fast velocity layer in the bottom 10-12 km under station GENI falls within that velocity range, further confirming our suspicion that magmatic intrusives do not pervade the lower crust.

The lack of a pervasive mafic lower crust under the Parnaíba basin may have implications

for understanding the depositional history of this basin. As outlined in Section 2, *Tozer et al. (2017)* have recently proposed that cratonic subsidence of the Parnaíba basin might be due to flexural bending driven by a buried load, and identified a postulated mafic lower crust for the Parnaíba block - along with sediment weight - as such buried load. The lack of a pervasive, high-density lower crustal body - as suggested by our S-velocity models - considerably reduces the load available for driving subsidence, and limits its ability to induce viscoelastic stress relaxation of the lithosphere (required to explain the long subsidence history of this basin). Alternatively, our smaller mafic body might be linked to a heating event ultimately responsible for basin subsidence. Indeed, *Daly et al. (2014)* found their results on the reflectivity structure of the Parnaíba basin to be consistent with thermal subsidence. However, we noticed that the large Vp/Vs ratios and the fast-velocity body in the lower crust coincide pretty closely with the location of the thickest cumulative isopachs for the Early Cretaceous Sardinha formation (see Figure 7), which makes us think that the fast lower-crustal body might have a similar origin. If our conclusion is correct, that would imply that the emplacement of the mafic body in the depocenter postdated the initiation of cratonic subsidence and invalidate the mafic layer as a valid remnant of the postulated heating event.

Convection processes in the deep mantle, on the other hand, have been shown to be capable of triggering vertical movements in the overlying lithosphere, and have been invoked to explain - for instance - the elevated topography of the South African Plateau (e.g. *Lithgow-Berteloni and Silver, 1998; Gurnis et al., 2000*). Similarly, cold-spots associated with convective downwellings may be capable of explaining the origin of regional subsidence (*Hartley and Allen, 1994*). Such downwellings have been invoked to explain the subsidence mechanism, for instance, of the Congo basin in Africa (*Downey et al., 2011*); after an initial

471 stage of uplift caused by isostatic rebound following delamination, a vertical downwelling
472 would have been caused by the sinking of the delaminated lithospheric fragment, which
473 would in turn drag the overlying lithosphere and cause subsidence of the initially elevated
474 region. *Tozer et al.* (2017) caution that precise constraints on the vertical emplacement
475 of the buried load are lacking, opening the possibility of such buried load to be emplaced
476 deeper in the mantle. Determination of lithospheric thickness, as well as imaging of the
477 sublithospheric mantle, is thus required to assess the plausibility of such mechanisms for the
478 Parnaíba basin.

479 Conclusions

480 We have developed 9 point estimates of crustal thickness and bulk Vp/Vs ratio across
481 the Parnaíba basin of NE Brazil, along with detailed velocity-depth profiles of S-velocity.
482 Our results are consistent with the presence of a mafic layer in the lower crust near the
483 depocenter of the basin, which is characterized by a thickness of 10-12 km and crustal S-
484 velocities varying between 4.0 and 4.2 km/s. The crustal architecture of the block is similar
485 to that of Precambrian terrains worldwide, suggesting minimal stretching of the basin's
486 underlying basement. Elastic flexure by a deep load is favored as a mechanism for the origin
487 and evolution of cratonic subsidence in the basin. However, such load cannot be attributed
488 to a pervasive intrusive body in the lower crust and propose deep mantle loads, perhaps
489 related to convective processes, as a more plausible candidates. Deep mantle structure,
490 nonetheless, needs to be investigated in order to assess the role of such deep convective
491 processes in the formation and evolution of this cratonic basin.

492 Acknowledgements

493 We thank an anonymous reviewer and the Associate Editor handling the submission, Dr.
494 Anthony Watts, for carefully reading the original manuscript and for constructive criticism
495 that significantly improved the discussion and presentation of our results. Acquisition and
496 analysis of the dataset presented in this study was funded through a grant awarded by BP
497 Energy do Brasil. Diogo L.O.C. additionally thanks BP Energy do Brasil for a generous
498 scholarship to complete his PhD degree at the Universidade Federal do Rio Grande do Norte.
499 Jordi Julià also thanks BP Energy do Brasil for awarding a research fellowship to conduct
500 this research.

501 **References**

- 502 Almeida, F.F.M., Hasui, Y., Brito Neves, B.B., Fuck, R.A. (1981). Brazilian structural
503 provinces: An introduction, *Earth Sci. Rev.*, **17**, 1-29.
- 504 Ammon, C.J. (1991). The isolation of receiver effects from teleseismic P waveforms,
505 *Bull. Seism. Soc. Am.*, **81**, 2504-2510.
- 506 Ammon, C. J., Randall, G.E., Zandt, G. (1990). On the non-uniqueness of receiver
507 function inversions, *J. Geophys. Res.*, **95**, 15,303-15,318.
- 508 Assumpção, M., Feng, M., Tassara, A., Julià, J. (2013a). Models of crustal thickness
509 for South America from seismic refraction, receiver functions and surface wave tomography,
510 *Tectonophysics*, **609**, 82-96.
- 511 Assumpção, M., Bianchi, M., Julià, J., Dias, F.L., França, G.S., Nascimento, R.M.N.,
512 Drouet, S., Pavão, C.S., Albuquerque, D.F., Lopes A.E.V. (2013b), Crustal thickness map
513 of Brazil: Data compilation and main features, *J. South Am. Earth Sci.*, **43**, 74-85.
- 514 Brito Neves, B.B., Fuck, R.A., Cordani, U.G., Thomas, A. (1984). Influence of basement
515 structures on the evolution of the major sedimentary basins of Brazil: A case of tectonic
516 heritage, *J. Geodyn.*, **1**, 495-510.
- 517 Brito Neves, B.B., Fuck, R.A. (2013). Neoproterozoic evolution of the basement of the
518 South American Platform, *J. South Am. Earth Sci.*, **47**, 72-89.
- 519 Cloetingh, S., Burov, E. (2011). Lithospheric folding and sedimentary basin evolution:
520 a review and analysis of formation mechanisms, *Basin Res.*, **23**, 257-290.
- 521 Christensen, N. I. (1996). Poissons ratio and crustal seismology, *J. Geophys. Res.*, **101**,
522 3139-3156.

- 523 Christensen, N.I., Mooney, W.D. (1995). Seismic velocity structure and composition of
524 the continental crust: A global view, *J. Geophys. Res.*, **100**, 9761-9788.
- 525 Cordani, U.G., Brito Neves, B.B., Fuck, R.A., Porto, R., Thomaz Filho, A., Cunha,
526 F.M.B. (1984). Estudo preliminar de integração do Pré-Cambriano com os eventos tectônicos
527 das bacias sedimentares brasileiras, *Ciência Técnica Petróleo, Seção Exploração de Petróleo*,
528 Rio de Janeiro 15, p70.
- 529 Cordani, U.G., Brito Neves, B.B., Thomaz Filho, A. (2009). Estudo preliminar de
530 integração do Pré-Cambriano com os eventos tectônicos das bacias sedimentares brasileiras
531 (Atualização), *Bol. Geociênc. Petrobras*, Rio de Janeiro **17** (1), 205-219.
- 532 Cordani, U.G., Pimentel, M.M., Araujo, C.E.G., Fuck, R.A. (2013). The significance of
533 the Transbrasiliano-Kandi tectonic corridor for the amalgamation of West Gondwana, *Braz.
534 J. Geol.*, **43**, 583-597.
- 535 Daly, M.C., Andrade, V., Barousse, C.A., Costa, R., McDowell, K., Piggot, N., Poole,
536 A.J. (2014). Brasiliano crustal structure and the tectonic setting of the Parnaíba basin of NE
537 Brazil: Results of a deep seismic reflection profile, *Tectonics*, **33**, doi:10.1002/2014TC003632.
- 538 de Castro, D.L., Fuck, R.A., Phillips, J.D., Vidotti, R.M., Bezerra, F.H.R., Dantas, E.L.
539 (2014). Crustal structure beneath the Paleozoic Parnaíba Basin revealed by airborne gravity
540 and magnetic data, Brazil, *Tectonophysics*, **614**, 128-145.
- 541 Downey, N., Gurnis, M., Avouac, J.-P. (2011). Subsidence history and geodynamic
542 evolution of the cratonic Congo Basin, *Geophys. Res. Abstracts*, **13**, EGU2011-388-1.
- 543 Durrheim, R. J., Mooney, W.D. (1991). Archean and Proterozoic crustal evolution:
544 Evidence from crustal seismology, *Geology*, **19**, 606-609.

- 545 Dziewonsky, A.M., Anderson, D.L. (1981). Preliminary reference earth model, *Phys.*
546 *Earth Planet. Int.*, **25**, 297-356.
- 547 Efron, B., Tibshirani, R. (1991). Statistical data analysis in the computer age, *Science*,
548 **253**, 390-395.
- 549 Feng, M., Assumpção, M., van der Lee, S. (2004). Group-velocity tomography and
550 lithospheric S-velocity structure of the South American continent, *Phys. Earth Planet.*
551 *Inter.*, **147**, 315-331.
- 552 Feng, M., Van der Lee, S., Assumpção (2007). Upper mantle structure of South America
553 from joint inversion of waveforms and fundamental-mode group velocities of Rayleigh waves,
554 *J. Geophys. Res.*, **112**, B04312, doi:10.1029/2006JB004449.
- 555 Fuck, R.A., Brito Neves, B.B., Schobbenhaus, C. (2008). Rodinia descendants in South
556 America, *Precambrian Res.*, **160**, 108-126.
- 557 Gilbert, A., Sheehan, A.F. (2004). Images of crustal variations in the intermountain
558 west, *J. Geophys. Res.*, **109**, 1978-2012.
- 559 Góes, A.M.O., Feijó, F.J. (1994), Bacia do Parnaíba, *Boletim de Geociências da Petro-*
560 *brás*, **8**, 57-67.
- 561 Góes, A.M.O., Travassos, W.A.S., Nunes, K.C. (1993). Projeto Parnaíba: Reavaliação
562 e perspectivas exploratórias, paper presented at Relatório Petrobras, DEXNOR-DINTER.
- 563 Gurnis, M., Mitrovica, J.X., Ritsema, J., van Heijst, H.J. (2000). Constraining mantle
564 density structure using geological evidence of surface uplift rates: The case of the African
565 Superplume, *Geochim. Geophys. Geosyst.*, **1**, 1999GC000035.
- 566 Hartley, R.W., Allen, P.A. (1994). Interior cratonic basins of Africa: Relation to conti-

- 567 nental break-up and role of mantle convection, *Basin Res.*, **6**, 95-113.
- 568 Julià, J., Ammon, C.J., Herrmann, R.B., Correig, A.M. (2000). Joint inversion of re-
569 ceiver functions and surface-wave dispersion ob- servations, *Geophys. J. Int.*, **143**, 99-112.
- 570 Julià, J., Ammon, C.J., Herrmann, R.B. (2003). Lithospheric structure of the Ara-
571 bian Shield from the joint inversion of receiver functions and surface-wave group velocities,
572 *Tectonophysics*, **371**, 1-21.
- 573 Julià, J. (2007). Constraining velocity and density contrasts across the crust mantle
574 boundary with receiver function amplitudes, *Geophys. J. Int.*, **171**, 286-301.
- 575 Julià, J., Assumpção, M., Rocha, M.P. (2008), Deep crustal structure of the Paraná
576 Basin from receiver functions and Rayleigh-wave dispersion: Evidence for a fragmented
577 cratonic root, *J. Geophys. Res.*, **113**, B08318, doi:10.1029/2007JB005374.
- 578 Kaminski, E., Jaupart, C. (2000). Lithosphere structure beneath the Phanerozoic in-
579 tracratonic basins of North America, *Earth Planet. Sci. Lett.*, **178**, 139-149.
- 580 Klein, G. deV., A.T. Hsui (1987) Origin of cratonic basins, *Geology*, **15**, 1094-1098.
- 581 Klein, E.L., Luzardo, R., Moura, C.A.V., Armstrong, R. (2008). Geochemistry and
582 zircon geochronology of Paleoproterozoic granitoids: further evidence on the magmatic and
583 crustal evolution of the São Luís cratonic fragment, Brazil, *Precambrian Res.*, **165**, 221-242.
- 584 Langston, C.A. (1979). Structure under Mount Rainier, Washington, inferred from tele-
585 seismic body waves, *J. Geophys. Res.*, **84**, 4749-4762.
- 586 Ligorría, J.P., Ammon, C.J. (1999). Iterative deconvolution and receiver function esti-
587 mation, *Bull. Seism. Soc. Am.*, **89**, 1395-1400.
- 588 Lithgow-Bertelloni, C., Silver, P.G. (1998), Dynamic topography, plate driving forces,

589 and the African superswell, *Nature*, **395**, 269-273.

590 Lloyd, S., van Der Lee, S., França, G.S., Assumpção, M., Feng, M. (2010). Moho map of
591 South America from receiver functions and surface waves, *J. Geophys. Res.*, **115**, B11315,
592 doi:10.1029/2009JB006829.

593 Luz, R.M.N., Julià, J., do Nascimento, A.F. (2015). Bulk crustal properties of the
594 Borborema Province, NE Brazil, from P-wave receiver functions: Implications for models of
595 intraplate Cenozoic uplift, *Tectonophysics*, **644-645**, 81-91.

596 McKenzie, D. (1978), Some remarks on the development of sedimentary basins, *Earth*
597 *Planet. Sci. Lett.*, **40**, 25-32.

598 Merle, R., Marzoli, A., Bertrand, H., Reisberg, L., Verati, C., Zimmermann, C., Chiara-
599 dia, M., Bellieni, G., Ernesto, M. (2011). $^{40}\text{Ar}/^{39}\text{Ar}$ ages and Sr-Nd-Pb-Os geochem-
600 istry of CAMP tholeiites from western Maranhão basin (NE Brazil), *Lithos*, **122**, 137-151,
601 doi:10.1016/j.lithos2010.12.010.

602 Nunes, K.C. (1993). Interpretação integrada da Bacia do Parnaíba com ênfase nos dados
603 aeromagnéticos, 3rd International Congress of the Brazilian Geophysical Society, Expanded
604 Abstracts, pp. 152-157.

605 Oliveira, D. C., Mohriak, W.U., (2003), Jaibaras Trough: An important element in the
606 early tectonic evolution of the Parnaíba interior sag basin, Northern Brazil, *Mar. Pet. Geol.*,
607 **20**, 351-383.

608 Owens, T.J., Zandt, G., Taylor, S.R. (1984). Seismic evidence for an ancient rift be-
609 neath the Cumberland Plateau, Tennessee: a detailed analysis of broadband teleseismic P
610 waveforms, *J. geophys. Res.*, **89**, 7783-7795.

- 611 Rossetti, D.F., Paz, J.D.S., Góes, A.M.O. (2004). Facies analysis of the Codó formation
612 (late Aptian) in the Grajaú area, southern São Luís-Grajaú Basin, An. Acad. Bras. Cienc.,
613 76, 791-806, doi:10.1590/S0001-37652004000400012.
- 614 Schimmel, M., Paulsen, H. (1997). Noise reduction and detection of weak, coherent
615 signals through phase-weighted stacks. *Geophys. J. Int.*, **130**, 497-505.
- 616 Tozer, B., Watts, A.B., Daly, M.C. (2017). Crustal structure, gravity anomalies, and
617 subsidence history of the Parnaíba cratonic basin, Northeast Brazil. *J. Geophys. Res.*, **122**,
618 doi:10.1002/2017JB014348.
- 619 Uieda, F., Barbosa V.L.F. (2017). Fast nonlinear gravity inversion in spherical coordi-
620 nates with application to the South American Moho, *Geophys. J. Int.*, **208**, 162-176.
- 621 van der Meijde, M., Julià, J., Assumpçao, M. (2013). Gravity derived Moho for South
622 America, *Tectonophysics*, **609**, 456-467.
- 623 Vaz, P.T., Rezende, N.A.M., Filho J.R.W., Travassos, W.A.S. (2007). Bacia do Parnaíba,
624 *Boletim de Geociências da Petrobrás*, textbf{2}, 253-263.
- 625 Zandt, G., Ammon, C.J. (1995). Continental crust composition constrained by measure-
626 ments of crustal Poisson's ratio, *Nature*, **374**, 152-154.
- 627 Zelt, B.C., Ellis, R.M. (1998). Receiver function studies in the Trans-Hudson orogen,
628 Saskatchewan, *Can. J. Earth Sci.*, **36**, 585-603.
- 629 Zhu, L., Kanamori, H. (2000). Moho depth variation in southern California from tele-
630 seismic receiver functions, *J. Geophys. Res.*, **105**, 2962-2980.

₆₃₁ **Tables**

Table 1: *Station coordinates and recording time windows for stations in the Parnaíba basin.*

| Station | Latitude | Longitude | Recording time |
|---------|----------|-----------|---------------------|
| | (deg) | (deg) | (YYYY.JJJ)* |
| BPPF | -6.2271 | -47.2518 | 2016.188 – 2017.199 |
| BUCO | -5.1586 | -43.2010 | 2016.118 – 2017.199 |
| GENI | -5.4612 | -45.5344 | 2016.105 – 2017.199 |
| GRJU | -5.8308 | -46.0882 | 2016.104 – 2017.199 |
| PRDT | -5.3241 | -44.3974 | 2016.106 – 2017.200 |
| STSN | -6.0787 | -46.5986 | 2016.105 – 2017.199 |
| STSР | -5.2889 | -43.8063 | 2016.119 – 2017.199 |
| TRZN | -5.1056 | -42.6344 | 2016.118 – 2017.199 |
| BDCO | -5.4517 | -45.0203 | 2015.222 – 2016.293 |

* Recording time window is given as year (YYYY) and Julian day (JJJ).

Table 2: $H\text{-}\kappa$ stacking parameters for varying values of Vp .

| Station | n | w1,w2,w3 | $H \pm 2\sigma$ (km) | | | | | $Vp/Vs \pm 2\sigma$ | | | |
|---------|-------------------|----------|----------------------|------------|------------|------------|------------|---------------------|-------------|-------------|-------------|
| | | | Vp 6.3 | Vp 6.4 | Vp 6.5 | Vp 6.6 | Vp 6.7 | Vp 6.3 | Vp 6.4 | Vp 6.5 | |
| 30 | BDCO | 17 | 0.4,0.3,0.3 | 41.9 ± 0.5 | 42.7 ± 0.5 | 43.7 ± 0.5 | 44.5 ± 0.5 | 45.5 ± 0.6 | 1.74 ± 0.02 | 1.73 ± 0.02 | 1.72 ± 0.02 |
| | BPPF [†] | 2 | 0.5,0.5,0.0 | 44.1 ± 0.2 | 45.0 ± 0.2 | 45.8 ± 0.2 | 46.7 ± 0.2 | 47.2 ± 0.2 | 1.74 ± 0.02 | 1.73 ± 0.02 | 1.73 ± 0.02 |
| | | 4 | 41.1 ± 1.3 | 41.9 ± 1.5 | 42.7 ± 1.5 | 43.6 ± 1.4 | 44.4 ± 1.5 | 1.75 ± 0.03 | 1.75 ± 0.03 | 1.74 ± 0.03 | 1.73 ± 0.03 |
| | BUCO | 21 | 0.4,0.3,0.3 | 37.8 ± 0.5 | 38.5 ± 0.6 | 39.3 ± 0.5 | 40.1 ± 0.4 | 40.9 ± 0.6 | 1.75 ± 0.02 | 1.74 ± 0.02 | 1.73 ± 0.02 |
| | GENI* | 4 | 0.5,0.5,0.0 | 42.1 ± 0.7 | 43.4 ± 0.8 | 45.1 ± 0.8 | 45.9 ± 0.9 | 46.8 ± 0.9 | 1.78 ± 0.03 | 1.78 ± 0.03 | 1.77 ± 0.03 |
| | GRJU | 28 | 0.4,0.3,0.3 | 42.1 ± 0.7 | 42.9 ± 0.7 | 43.6 ± 0.7 | 44.5 ± 0.7 | 45.3 ± 0.7 | 1.78 ± 0.02 | 1.78 ± 0.03 | 1.78 ± 0.02 |
| | PRDT | 19 | 0.4,0.3,0.3 | 39.5 ± 1.5 | 40.2 ± 2.1 | 41.1 ± 1.9 | 42.0 ± 2.0 | 42.8 ± 1.8 | 1.78 ± 0.06 | 1.78 ± 0.06 | 1.77 ± 0.07 |
| | STSN | 24 | 0.4,0.3,0.3 | 40.5 ± 0.8 | 41.3 ± 0.9 | 42.2 ± 0.7 | 43.1 ± 0.7 | 43.9 ± 1.0 | 1.75 ± 0.02 | 1.73 ± 0.02 | 1.73 ± 0.02 |
| | STSР | 20 | 0.4,0.3,0.3 | 38.4 ± 0.4 | 39.2 ± 0.4 | 40.0 ± 0.4 | 40.7 ± 0.4 | 41.5 ± 0.5 | 1.71 ± 0.01 | 1.71 ± 0.01 | 1.70 ± 0.01 |
| | TRZN | 22 | 0.4,0.3,0.3 | 38.7 ± 1.1 | 39.5 ± 0.9 | 40.3 ± 1.1 | 41.0 ± 0.7 | 41.8 ± 1.3 | 1.73 ± 0.03 | 1.72 ± 0.03 | 1.71 ± 0.03 |

The table includes the number of waveforms (n), P-wave velocity assumed (Vp) in km/s, and weights for the Ps (w1), PpPs (w2), and PpSs + PsPs (w3) phases, respectively.

* Results for station GENI are restricted to events approaching the station at $\sim 293^\circ$ back-azimuth.

[†] Results for station BPPF are restricted to events approaching the station at $\sim 166^\circ$ (top) and $\sim 294^\circ$ (bottom) back-azimuth.

632 **Figure Captions**

633 **Figure 1** - Geological map of the Parnaíba basin displaying the location of Parnaíba
634 Basin Analysis Project (PBAP) stations (triangles) utilized in this study. AM - Amazonian
635 Craton; BB - Borborema Province; SF - São Francisco Craton; SL - São Luís Craton; TO -
636 Tocantins Province.

637 **Figure 2** - Receiver function stacks developed for the seismic stations in the Parnaíba
638 basin. Top and bottom traces refer to radial and transversal receiver functions, respectively.
639 The number of waveforms included in the stack, average back-azimuth, and average ray
640 parameter are displayed in the upper right corner of each panel. The stacks are presented
641 through a black line within a gray shade representing 1σ -confidence bounds for the stacked
642 amplitudes.

643 **Figure 3** - Sample H- κ stacking results for station STSR and GRJU. The top panels
644 display the H κ stacking surfaces, while the bottom panels display the corresponding radial
645 receiver functions utilized during the stacking procedure, sorted by ray parameter. The
646 thick, red line in the top panels is the 1σ -confidence ellipse from bootstrapping, and the
647 thin, red lines in the bottom panels are the phase moveout curves for the Ps, PpPs and
648 PpSs+PsPs phases associated to the maximum in the H κ -stacking surface.

649 **Figure 4** - H- κ stacking results for Vp/Vs ratio (top) and crustal thickness (bottom)
650 for all the stations in the Parnaíba basin. The vertical lines represent 2σ confidence bounds,
651 while the red stripes mark the regions of 1.70-1.72 and 40-42 km variation in Vp/Vs ratio
652 and crustal thickness, respectively. Note the thickening and increase in Vp/Vs ratio around
653 stations GRJU, GENI, and BDCO.

654 **Figure 5** - Joint inversion results for stations GRJU (left) and STSR (right). Com-

parison between observed (black) and predicted (red) receiver functions are shown in the upper-left panels, while comparison between observed (black triangles) and predicted (red line) group velocities are shown in the lower-left panels. The inverted (black line) and initial (blue line) S-velocity models are displayed in the right panels, along with the 2σ -confidence bounds for the inverted velocities (grey band). The numbers next to the receiver function waveforms indicate the number of waveforms (n), the average back-azimuth (baz) and standard deviation (sdbaz), and the average ray parameter (rayp) and standard deviation (sdrayp), according to (n) baz|pmsdbaz rayp±sdrayp.

Figure 6 - Joint inversion S-velocity models for each station along the profile, sorted according to station location. Inverted models are shown as black lines, with grey bands marking the 2σ -confidence bounds. H- κ stacking results for crustal thickness are superimposed as red, transparent bands, for comparison. The main layer boundaries for the sediment-bedrock interface (purple), the upper-lower crust interface (blue) and crust-mangle boundary (green) from the seismic and gravity model of *Tozer et al. (2017)* have been superimposed to the velocity models. Note the thicker crust under stations GRJU, GENI, and BDCO, predicted by the joint inversion models.

Figure 7 - Cumulative isopach map for the Sardinha Formation with the location of our seismic stations superimposed. The Figure also displays the location of the seismic reflection line of *Daly et al. (2014)*, along with the location of the Mid Crustal Reflector (MCR) imaged in their study. Note how stations GRJU, GENI, and BDCO are located on top of the thickest magmatic accumulation.

Article text

[Click here to download Article text blank.docx](#)

676 **Figures**

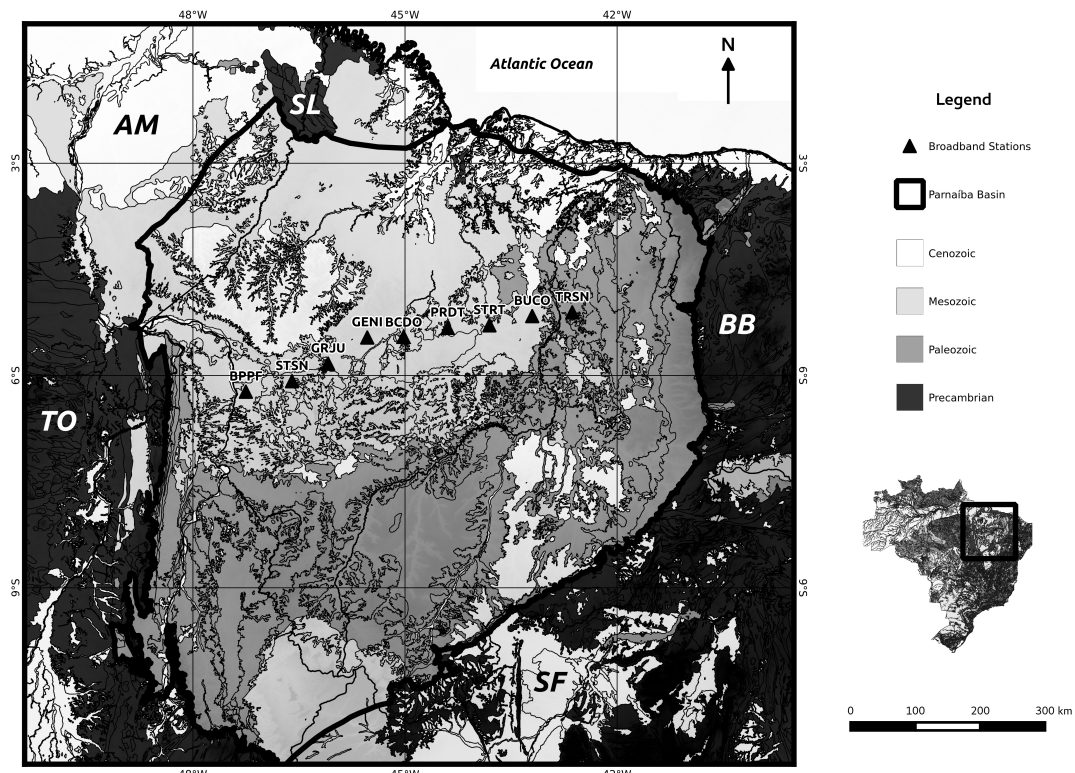


Figure 1: Geological map of the Parnaíba basin displaying the location of Parnaíba Basin Analysis Project (PBAP) stations (triangles) utilized in this study. AM - Amazonian Craton; BB - Borborema Province; SF - São Francisco Craton; SL - São Luís Craton; TO - Tocantins Province.

Figure 02

[Click here to download Figure figure02.pdf](#)

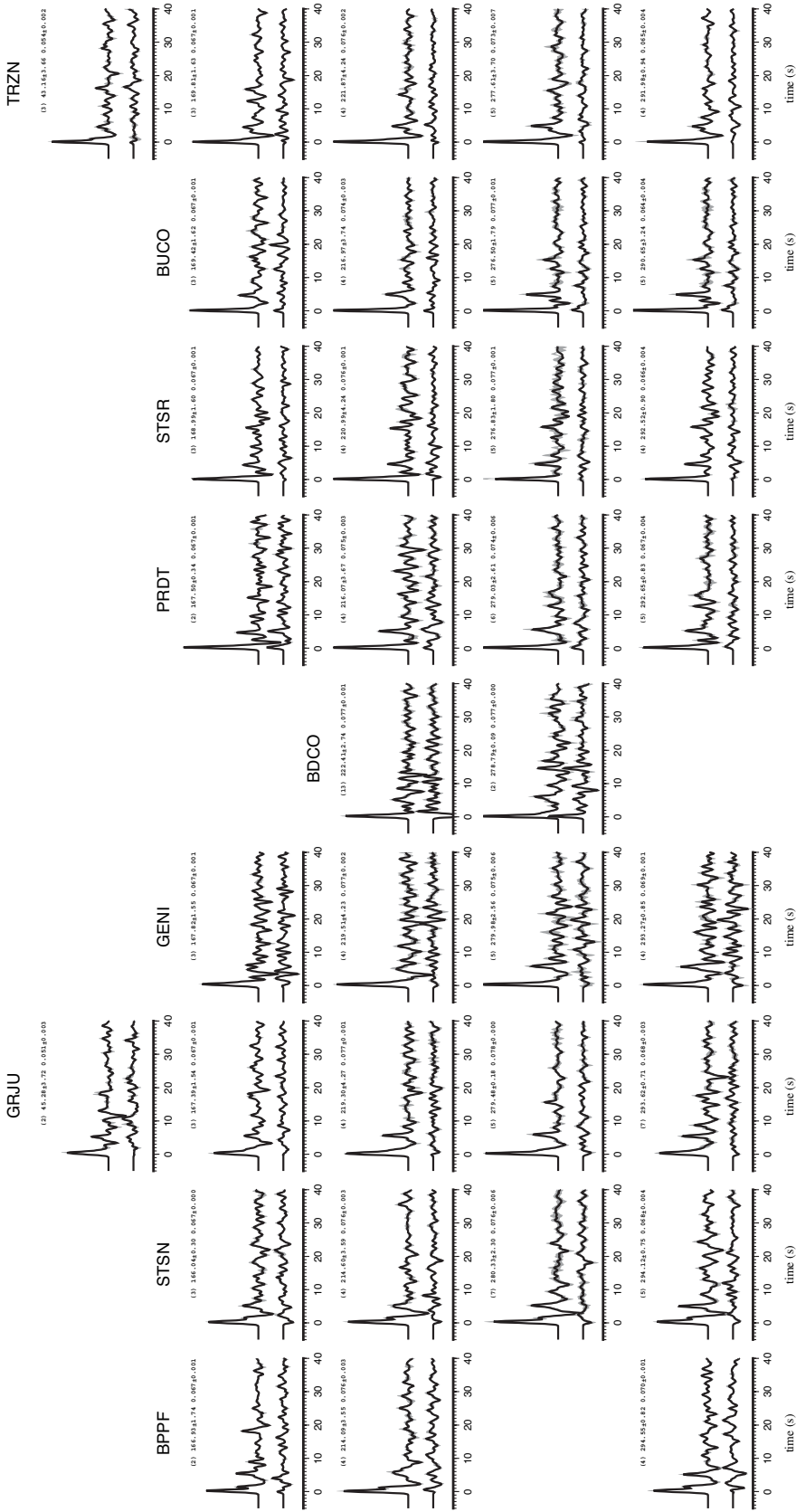


Figure 2: Receiver function stacks developed for the seismic stations in the Parnaíba basin. Top and bottom traces refer to radial and transversal receiver functions, respectively. The number of waveforms included in the stack, average back-azimuth, and average ray parameter are displayed in the upper right corner of each panel. The stacks are presented through a black line within a gray shade representing 1σ -confidence bounds for the stacked amplitudes.

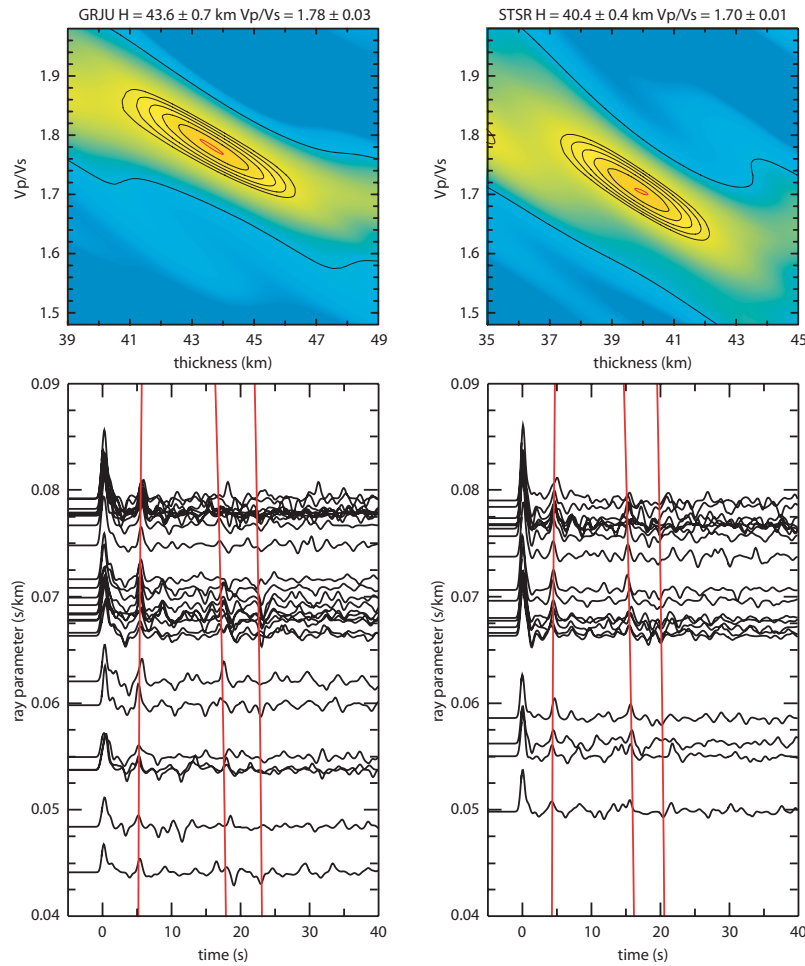


Figure 3: Sample $H\kappa$ stacking results for station STSR and GRJU. The top panels display the $H\kappa$ stacking surfaces, while the bottom panels display the corresponding radial receiver functions utilized during the stacking procedure, sorted by ray parameter. The thick, red line in the top panels is the 1σ -confidence ellipse from bootstrapping, and the thin, red lines in the bottom panels are the phase moveout curves for the Ps , $PpPs$ and $PpSs+PsPs$ phases associated to the maximum in the $H\kappa$ -stacking surface.

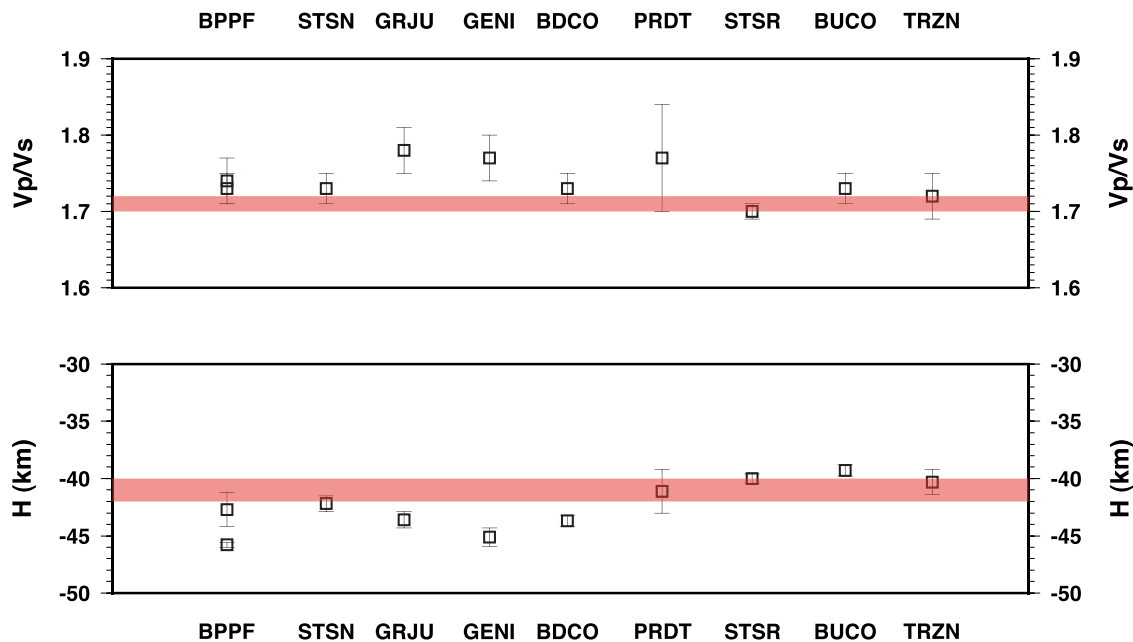


Figure 4: H - κ stacking results for V_p/V_s ratio (top) and crustal thickness (bottom) for all the stations in the Parnaíba basin. The vertical lines represent 2σ confidence bounds, while the red stripes mark the regions of 1.70-1.72 and 40-42 km variation in V_p/V_s ratio and crustal thickness, respectively. Note the thickening and increase in V_p/V_s ratio around stations GRJU, GENI, and BDCO.

Figure 05

[Click here to download Figure figure05.pdf](#)

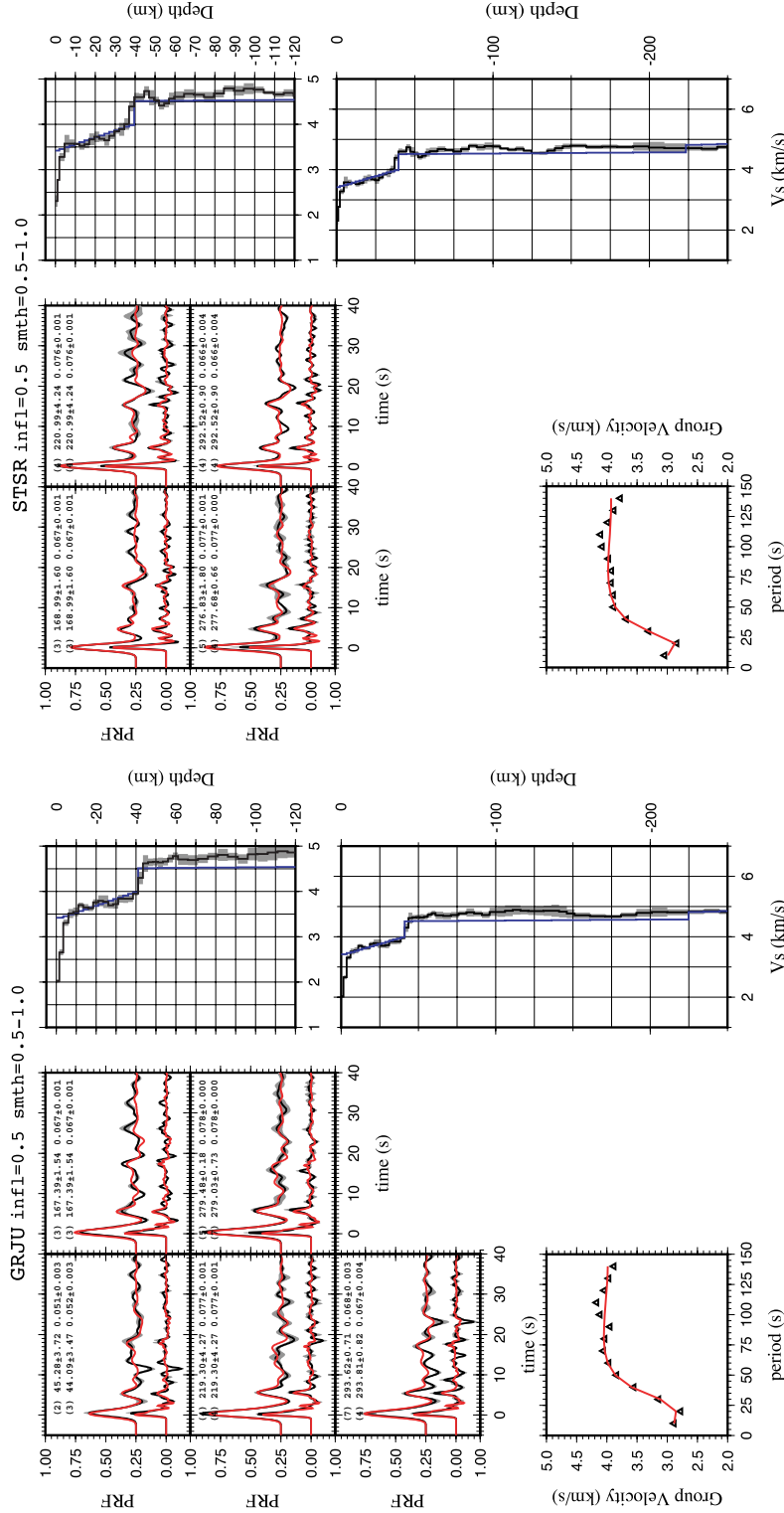


Figure 5: Joint inversion results for stations GRJU (left) and STSR (right). Comparison between observed (black) and predicted (red) receiver functions are shown in the upper-left panels, while comparison between observed (black triangles) and initial (blue line) S-velocity models are displayed in the right panels, along with the 2σ -confidence bounds for the inverted velocities (grey band). The numbers next to the receiver function waveforms indicate the number of waveforms (n), the average back-azimuth (baz) and standard deviation ($s\text{d}\text{baz}$), and the average ray parameter ($s\text{d}\text{ray}$) and standard deviation ($s\text{d}\text{ray}\pm s\text{d}\text{ray}$.

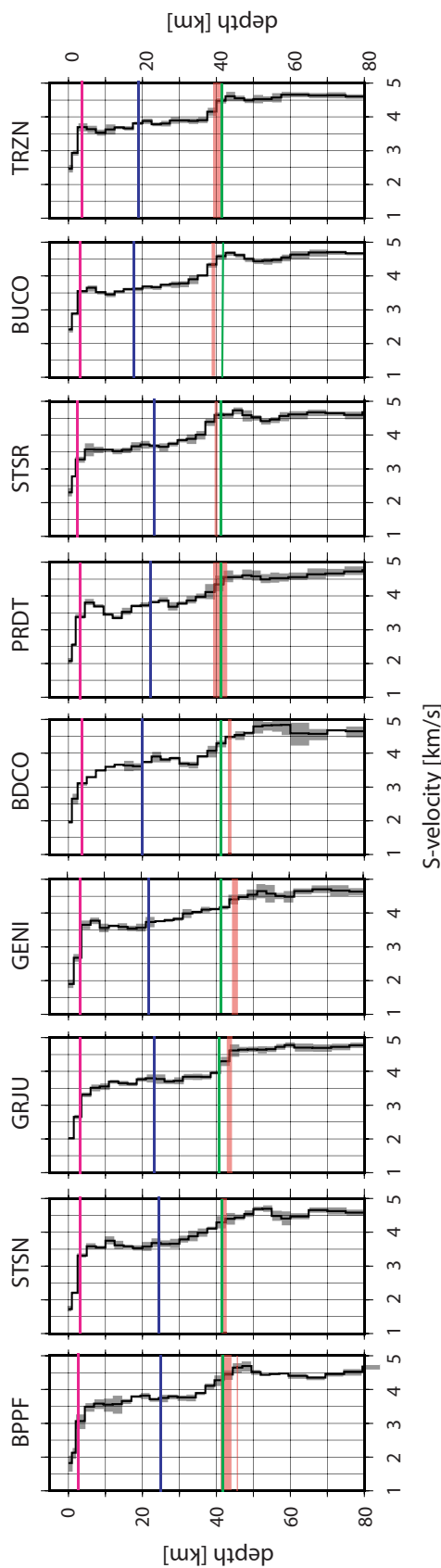


Figure 6: Joint inversion S-velocity models for each station along the profile, sorted according to station location. Inverted models are shown as black lines, with grey bands marking the 2σ -confidence bounds. $H\text{-}\kappa$ stacking results for crustal thickness are superimposed as red, transparent bands, for comparison. The main layer boundaries for the sediment-bedrock interface (purple), the upper-lower crust interface (blue) and crust-mantle boundary (green) from the seismic and gravity model of Tozer et al. (2017) have been superimposed to the velocity models. Note the thicker crust under stations GRJU, GENI, and BDCO, predicted by the joint inversion models.

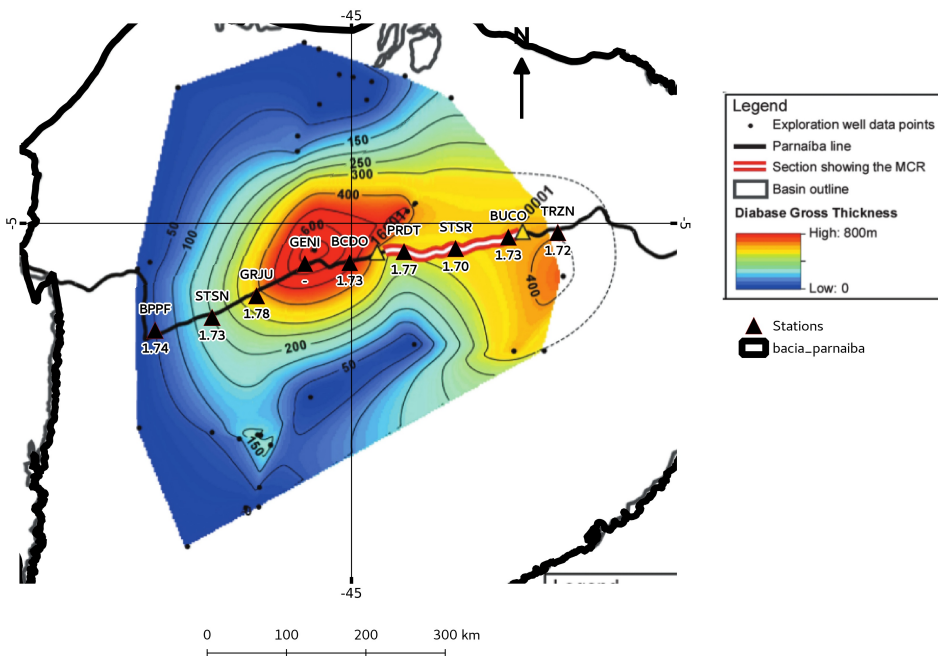


Figure 7: Cumulative isopach map for the Sardinha Formation with the location of our seismic stations superimposed. The Figure also displays the location of the seismic reflection line of Daly et al. (2014), along with the location of the Mid Crustal Reflector (MCR) imaged in their study. Note how stations GRJU, GENI, and BDCO are located on top of the thickest magmatic accumulation.

Capítulo 5

Artigo: Receiver function imaging of mantle transition zone discontinuities beneath Parnaíba Basin

Essa seção corresponde a segunda etapa do projeto, a qual consiste em observar as descontinuidades mantélicas de 410 km e 660 km, limites inferior e superior da Zona de Transição, abaixo da bacia do Parnaíba com as funções do receptor. Os limites da Zona de Transição e sua espessura são dependentes da temperatura, logo quando estão associados a anomalias termais essas descontinuidades de 410 km e 660 km devem ser imageadas a uma profundidade diferente da convencionada pelos modelos de velocidade globais. Para isso, apresentaremos empilhamentos e a migração em profundidade das funções do receptor para 9 estações na transecta NW-SE na parte central da bacia, como pode ser visto na Figura 5.1.

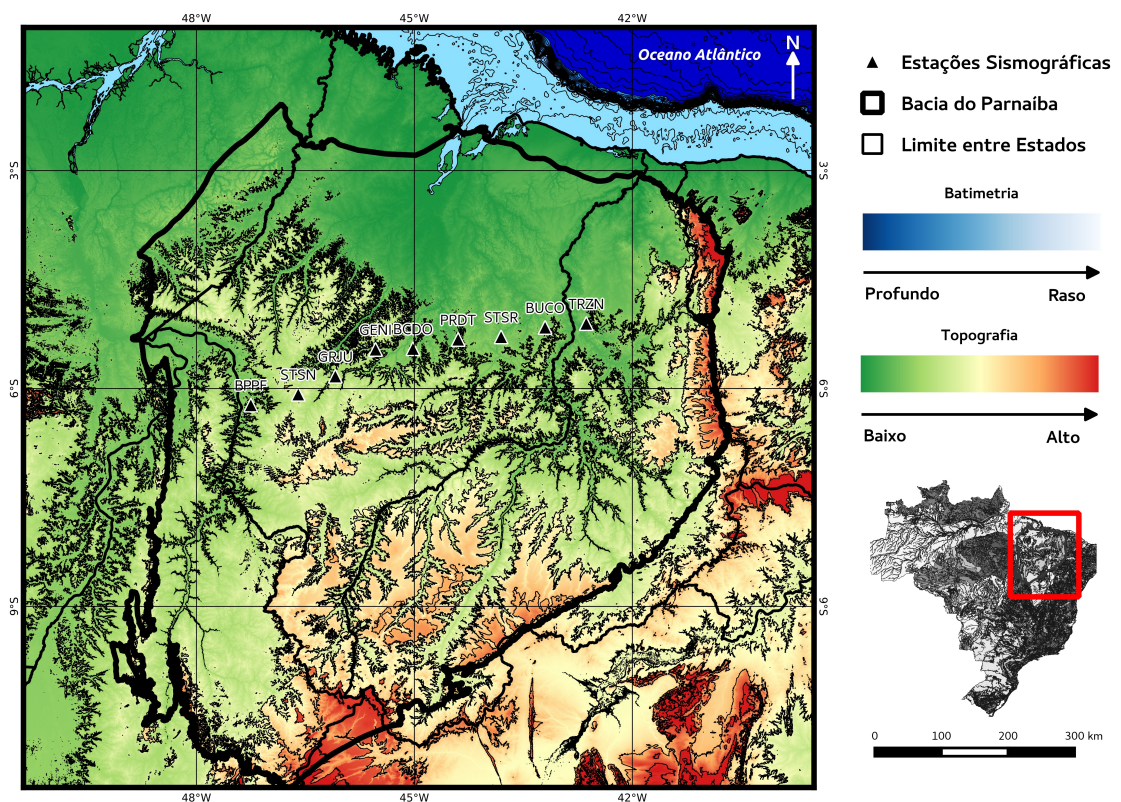


Figura 5.1: Mapa com as estações da rede da BP na transecta NE-SW na Bacia do Parnaíba.

Capítulo 6

Artigo: Ambient noise tomography across Parnaíba Basin

Essa seção corresponde a terceira etapa do projeto, a qual consiste em calcular as velocidades de propagação das ondas de superfície através da correlação do ruído sísmico ambiental e procurar um modelo que melhor se ajuste às anomalias de velocidades encontradas. Nesta parte do trabalho iremos utilizar um banco de dados maior, envolvendo estações de 4 redes sismográficas diferentes. Esse banco de dados consiste de um total de 31 estações de banda larga provenientes das redes RSBR (Rede Sismográfica Brasileira), RSISNE (Rede Sismográfica do Nordeste do Brasil), BODES (estações instaladas entre 2014 e 2016 numa transecta N-S na Província Borborema) e BP (rede utilizada nas estapas anteriores). Uma feição interessante que será o foco nessa etapa é o Lineamento Transbrasiliense, descontinuidade de magnitude continental situada entre o Cráton Amazônico e a porção leste da Plataforma Sul-Americana. O objetivo principal desse trabalho é imagear essa mega-estrutura dentro da bacia, pois a subsidência e a deposição estão fortemente ligadas a essa estrutura [Vaz et al., 2007].

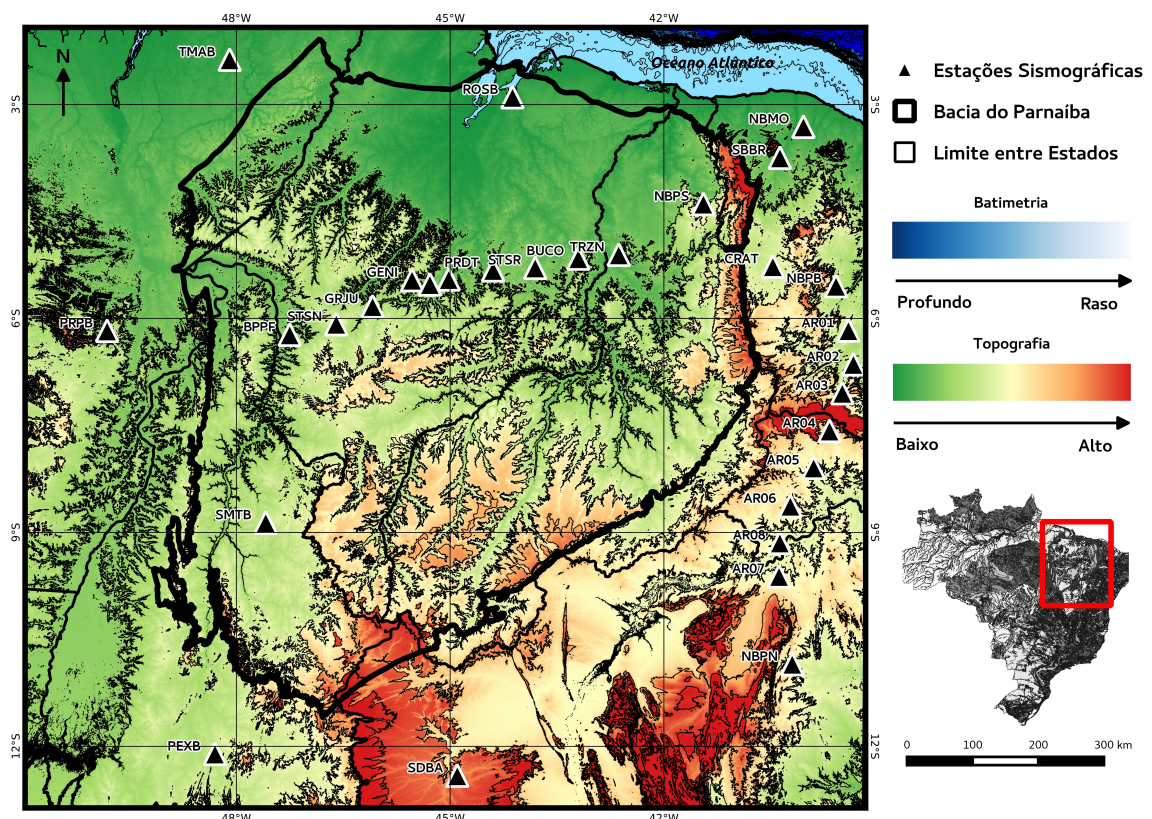


Figura 6.1: Mapa com as estações da rede da BP, BODES, RSISNE e RSBR na Bacia do Parnaíba e na sua vizinhança.

Bibliografia

Philip A. Allen and John J. Armitage. Cratonic Basins. In Cathy Busby and Antonio Azor, editors, *Tectonics of Sedimentary Basins*, pages 602–620. John Wiley & Sons, Ltd, 2012. ISBN 9781444347166. URL <http://onlinelibrary.wiley.com/doi/10.1002/9781444347166.ch30/summary>. DOI: 10.1002/9781444347166.ch30.

John Armitage and Philip Allen. Cratonic basins and the long-term subsidence history of continental interiors. *Journal of the Geological Society*, 167:61–70, 2010. ISSN 0016-7649. doi: 10.1144/0016-76492009-108.

Marcelo Assumpção, Marcelo Bianchi, Jordi Julià, Fábio L. Dias, George Sand França, Rosana Nascimento, Stéphane Drouet, César Garcia Pavão, Diogo Farrapo Albuquerque, and Afonso E. V. Lopes. Crustal thickness map of brazil: Data compilation and main features. *Journal of South American Earth Sciences*, 43:74–85, 2013a. ISSN 0895-9811. doi: 10.1016/j.jsames.2012.12.009. URL <http://www.sciencedirect.com/science/article/pii/S0895981113000059>.

Marcelo Assumpção, Mei Feng, Andrés Tassara, and Jordi Julià. Models of crustal thickness for south america from seismic refraction, receiver functions and surface wave tomography. *Tectonophysics*, 609:82–96, 2013b. ISSN 0040-1951. doi: 10.1016/j.tecto.2012.11.014. URL <http://www.sciencedirect.com/science/article/pii/S0040195112007330>.

B.B. Brito Neves, R.A. Fuck, U.G. Cordani, and F.A. Thomaz. Influence of basement structures on the evolution of the major sedimentary basins of brazil: A case of tectonic heritage. *Journal of Geodynamics*, 1(3):495–510, 1984. ISSN 02643707. doi: 10.1016/0264-3707(84)90021-8. URL <http://linkinghub.elsevier.com/retrieve/pii/0264370784900218>.

U.G. Cordani, B.B. Brito Neves, and Thomaz Filho A. Estudo preliminar de integração do pré-cambriano com os eventos tectônicos das bacias sedimentares brasileiras(atualização). *Boletim de Geociências da Petrobras*, 17(1):205–219, 2009.

Michael C. Daly, Vander Andrade, Chuck A. Barousse, Rafaela Costa, Kenneth McDowell, Neil Piggott, and Alan J. Poole. Brasiliano crustal structure and the tectonic setting of the parnaíba basin of NE brazil: Results of a deep seismic reflection profile. *Tectonics*, 33(11):2014TC003632, 2014. ISSN 1944-9194. doi: 10.1002/2014TC003632. URL <http://onlinelibrary.wiley.com/doi/10.1002/2014TC003632/abstract>.

David L. de Castro, Reinhardt A. Fuck, Jeffrey D. Phillips, Roberta M. Vidotti, Francisco H. R. Bezerra, and Elton L. Dantas. Crustal structure beneath the paleozoic parnaíba basin revealed by airborne gravity and magnetic data, brazil. *Tectonophysics*, 614:128–145, 2014. ISSN 0040-1951. doi: 10.1016/j.tecto.2013.12.009. URL <http://adsabs.harvard.edu/abs/2014Tectp.614..128D>.

David Lopes de Castro, Francisco Hilário Bezerra, Reinhardt Adolfo Fuck, and Roberta Mary Vidotti. Geophysical evidence of pre-sag rifting and post-rifting fault reactivation in the parnaíba basin, brazil. *Solid Earth*, 7(2):529–548, 2016. ISSN 1869-9510. doi: 10.5194/se-7-529-2016. URL <http://www.solid-earth.net/7/529/2016/se-7-529-2016-discussion.html>.

Diógenes Custódio de Oliveira and Webster Ueipass Mohriak. Jaibaras trough: an important element in the early tectonic evolution of the parnaíba interior sag basin, northern brazil. *Marine and Petroleum Geology*, 20(3-4):351–383, March 2003. ISSN 02648172. doi: 10.1016/S0264-8172(03)00044-8. URL <http://linkinghub.elsevier.com/retrieve/pii/S0264817203000448>.

Mei Feng, Marcelo Assumpção, and Suzan Van der Lee. Group-velocity tomography and lithospheric s-velocity structure of the south american continent. *Physics of the Earth and Planetary Interiors*, 147(4):315–331, 2004. ISSN 0031-9201. doi: 10.1016/j.pepi.2004.07.008. URL <http://www.sciencedirect.com/science/article/pii/S0031920104002924>.

Mei Feng, Suzan van der Lee, and Marcelo Assumpção. Upper mantle structure of south america from joint inversion of waveforms and fundamental mode group velocities of rayleigh waves. *Journal of Geophysical Research*,

112:B04312, 2007. ISSN 2156-2202. doi: 10.1029/2006JB004449. URL <http://onlinelibrary.wiley.com/doi/10.1029/2006JB004449/abstract>.

Reinhardt A. Fuck, Benjamim Bley Brito Neves, and Carlos Schobbenhaus. Rodinia descendants in south america. *Precambrian Research*, 160(1):108–126, 2008. ISSN 0301-9268. doi: 10.1016/j.precamres.2007.04.018. URL <http://www.sciencedirect.com/science/article/pii/S0301926807001593>.

Bruno Goutorbe, Diogo Luiz de Oliveira Coelho, and Stéphane Drouet. Rayleigh wave group velocities at periods of 6–23 s across brazil from ambient noise tomography. *Geophysical Journal International*, 203(2):869–882, November 2015. ISSN 0956-540X, 1365-246X. doi: 10.1093/gji/ggv343. URL <http://gji.oxfordjournals.org/content/203/2/869>.

A.M.O. Góes and F.J. Feijó. Bacia do parnaíba. *Boletim de Geociências da Petrobras*, 8:57–67, 1994.

Ana Maria Góes. *Formação Poti (Carbonífero inferior) da Bacia do Parnaíba*. text, Universidade de São Paulo, September 1995. URL <http://www.teses.usp.br/teses/disponiveis/44/44136/tde-11022014-105309/>. DOI: 10.11606/T.44.1995.tde-11022014-105309.

Roxby W. Hartley and Philip A. Allen. Interior cratonic basins of africa: relation to continental break-up and role of mantle convection. *Basin Research*, 6(2):95–113, 1994. ISSN 1365-2117. doi: 10.1111/j.1365-2117.1994.tb00078.x. URL <http://onlinelibrary.wiley.com/doi/10.1111/j.1365-2117.1994.tb00078.x/abstract>.

Edouard Kaminski and Claude Jaupart. Lithosphere structure beneath the phanerozoic intracratonic basins of north america. *Earth and Planetary Science Letters*, 178 (1):139–149, 2000. ISSN 0012-821X. doi: 10.1016/S0012-821X(00)00067-4. URL <http://www.sciencedirect.com/science/article/pii/S0012821X00000674>.

Simon Lloyd, Suzan van der Lee, George Sand França, Marcelo Assumpção, and Mei Feng. Moho map of south america from receiver functions and surface waves. *Journal of Geophysical Research: Solid Earth*, 115 (B11):n/a–n/a, 2010. ISSN 2156-2202. doi: 10.1029/2009JB006829. URL <http://onlinelibrary.wiley.com/doi/10.1029/2009JB006829/abstract>.

Dan McKenzie. Some remarks on the development of sedimentary basins. *Earth and Planetary Science Letters*, 40(1):25–32, June 1978. ISSN 0012-821X. doi: 10.1016/0012-821X(78)90071-7. URL <http://www.sciencedirect.com/science/article/pii/0012821X78900717>.

Dan McKenzie and Keith Priestley. Speculations on the formation of cratons and cratonic basins. *Earth and Planetary Science Letters*, 435(Supplement C):94–104, February 2016. ISSN 0012-821X. doi: 10.1016/j.epsl.2015.12.010. URL <http://www.sciencedirect.com/science/article/pii/S0012821X15007736>.

Renaud Merle, Andrea Marzoli, Hervé Bertrand, Laurie Reisberg, Chrystèle Verati, Catherine Zimmermann, Massimo Chiaradia, Giuliano Bellieni, and Marcia Ernesto. 40ar/39ar ages and sr–nd–pb–os geochemistry of camp tholeiites from western maranhão basin ne brazil. *Lithos*, 122(3–4):137–151, March 2011. ISSN 0024-4937. doi: 10.1016/j.lithos.2010.12.010. URL <https://www.sciencedirect.com/science/article/pii/S0024493710003531>.

Leonardo Silva Ribeiro Mocitaiba, David Lopes de Castro, and Diógenes Custódio de Oliveira. Cartografia geofísica regional do magmatismo mesozoico na bacia do parnaíba. *Geologia USP. Série Científica*, 17(2):169–192, August 2017. ISSN 2316-9095. doi: 10.11606/issn.2316-9095.v17-455. URL <http://www.revistas.usp.br/guspsc/article/view/134870>.

B. Tozer, A. B. Watts, and M. C. Daly. Crustal structure, gravity anomalies, and subsidence history of the parnaíba cratonic basin, northeast brasil. *Journal of Geophysical Research: Solid Earth*, 122(7):2017JB014348, July 2017. ISSN 2169-9356. doi: 10.1002/2017JB014348. URL <http://onlinelibrary.wiley.com/doi/10.1002/2017JB014348/abstract>.

Leonardo Uieda and Valéria C. F. Barbosa. Fast nonlinear gravity inversion in spherical coordinates with application to the south american moho. *Geophysical Journal International*, 208(1):162–176, 2017. ISSN 0956-540X. doi: 10.1093/gji/ggw390. URL <https://academic.oup.com/gji/article-abstract/208/1/162/2417303/Fast-nonlinear-g>

M. van der Meijde, J. Julià, and M. Assumpção. Gravity derived moho for south america. *Tectonophysics*, 609:456–467, 2013. ISSN 0040-1951. doi: 10.1016/j.tecto.2013.03.023. URL <http://www.sciencedirect.com/science/article/pii/S0040195113001972>.

P.T. Vaz, N.A.M. Rezende, Filho J.R. W., and W.A.S. Travassos. Bacia do parnaíba.
Boletim de Geociências da Petrobras, 15(2):253–263, 2007.